

**ON DESIGN OF TUNABLE LEAKY WAVEGUIDE  
ANTENNAS FOR A LARGE FORMAT LENS BASED  
FOCAL PLANE ARRAY WITH WIDE SCANNING  
CAPABILITIES**



**ON DESIGN OF TUNABLE LEAKY WAVEGUIDE  
ANTENNAS FOR A LARGE FORMAT LENS BASED  
FOCAL PLANE ARRAY WITH WIDE SCANNING  
CAPABILITIES**

**Thesis**

to obtain the degree of

**Master of Science**

in Electrical Engineering

at Delft University of Technology,

to be defended on 07th November, 2023 at 14:00.

by

**Muhan ZHANG**

This thesis has been approved by the

supervisor: prof. dr. N. Llombart Juan  
daily supervisor: dr. S.O. Dabironezare

Composition of committee:

Prof. dr. N. Llombart Juan,	Delft University of Technology
Dr. B.J. Kooij,	Delft University of Technology
Dr. S.O. Dabironezare,	Delft University of Technology



*Keywords:* Focal plane arrays, lens antennas, Coherent Fourier Optics, spectral techniques, sub-millimetre wavelengths.

Copyright © 2023 by M. Zhang

An electronic version of this dissertation is available at  
<http://repository.tudelft.nl/>.

*There is only one heroism in the world:  
to see the world as it is and to love it.*

Romain Rolland



# CONTENTS

<b>List of Figures</b>	<b>ix</b>
<b>List of Tables</b>	<b>xi</b>
<b>1 Introduction</b>	<b>1</b>
1.1 Application: Imaging Radars at 340GHz. . . . .	1
1.2 Goal: Study the Performance of a Lens Focal Plane Array Architecture with LW Feeds . . . . .	3
1.3 Geometry and Principle of the LW Antenna . . . . .	3
<b>2 Array Synthesis Methodology</b>	<b>5</b>
2.1 Antenna in Reception Methodology for Analysing Quasi-Optical Systems . . . . .	5
2.2 Coherent Fourier Optics: Coupling of the Reflector to the Lens Based Focal Plane Array . . . . .	7
2.3 Spectral Green's Function: Radiation Pattern of Leaky Wave Feeders . . . . .	8
2.3.1 Single-Layer Model . . . . .	9
2.3.2 Double-Layer Model . . . . .	9
2.4 Improving the Scan Loss Performance of a QO System via Phase Matching in Reception . . . . .	10
<b>3 CFO Design of the focal plane array with shaped lens surfaces</b>	<b>11</b>
3.1 CFO with a Gaussian Feed: Description of Three Regions in a Large Format Focal Plane Array . . . . .	11
3.1.1 Region 1: Homogeneous Lens Array with Identical Feeders . . . . .	11
3.1.2 Region 2: Homogeneous Lens Array with Displaced Feeders. . . . .	12
3.1.3 Region 3: Non-Homogeneous Lens Array . . . . .	12
3.1.4 Region 4: Non-Homogeneous Array with Shaped Lens Surface . . . . .	13
3.2 Application Case: Large Format FPA in an Imaging Radar at 340GHz . . . . .	13
3.3 Modelling the Antenna Feeder inside Each Lens Element as a Gaussian Feed . . . . .	14
<b>4 Synthesising the pattern of the leaky wave feeder</b>	<b>15</b>
4.1 Lens Feeder Geometry . . . . .	15
4.2 Field Matching to the Gaussian Beam. . . . .	17
4.2.1 Definition . . . . .	17
4.2.2 Case 1: Silicon Top . . . . .	17
4.2.3 Case 2: HDPE Top . . . . .	19
4.3 Leaky Wave Geometry . . . . .	20
4.3.1 Case 1: Scanning Broadside . . . . .	20
4.3.2 Case 2: Scanning 24 Beams . . . . .	21

4.3.3	Case 3: Scanning 50 Beams . . . . .	21
4.4	Asymmetric Leaky Wave Patterns Using Tunable Resonant Cavities. . . . .	23
4.4.1	Trade Off due to Permittivity of the Cavity . . . . .	23
<b>5</b>	<b>Synthesis of the Large Format Lens based Focal Plane Array</b>	<b>27</b>
5.1	Representing the Lens Surface Using the Zernike Expansion . . . . .	27
5.2	Importing the Lens Shape to 3D Electromagnetic Design Software . . . . .	28
5.2.1	Choosing Representative Points and Giving the Lens Size . . . . .	29
5.2.2	Generating Zernike Matrix in MATLAB. . . . .	30
5.2.3	Importing .zer Files from MATLAB into GRASP . . . . .	30
5.2.4	Importing .stp Files from GRASP into CST . . . . .	30
5.2.5	Importing .stp Files from CST into AutoCAD . . . . .	30
5.2.6	Rotating the Model According to the Position . . . . .	31
5.3	3D CAD View of the Entire FPA with the Reflector. . . . .	31
<b>6</b>	<b>Validation using Commercial Simulators</b>	<b>33</b>
6.1	Evaluating the Performance of the Lens Antenna Elements Using CST . . . . .	33
6.1.1	Case 1: Scanning Broadside . . . . .	33
6.1.2	Case 2: Scanning 24 Beams . . . . .	34
6.1.3	Case 3: Scanning 50 Beams . . . . .	34
6.2	Evaluating the Performance of One Lens Antenna Element with Displaced Feeder and Shaped Surface Using CST . . . . .	36
6.2.1	Feeder at the Focus of the Lens . . . . .	36
6.2.2	Displaced Feeder over the Lens Focal Plane . . . . .	38
6.2.3	Shaped Lens Surface with and without a Matching layer . . . . .	38
6.3	Evaluating the Performance of the Complete QO System using CST and TICRA GRASP . . . . .	38
<b>7</b>	<b>Conclusion</b>	<b>43</b>
7.1	Summary and Conclusion . . . . .	43
7.2	Future Outlook . . . . .	44
	<b>Acknowledgements</b>	<b>45</b>
	<b>List of Publications</b>	<b>47</b>
	<b>References</b>	<b>49</b>

# LIST OF FIGURES

1.1	An illustration of the large format lens based FPA and the geometry of the leaky wave feeders [1]. . . . .	3
2.1	Transmission line model. . . . .	9
2.2	Scan loss of the QO system versus the number of beams scanned by the primary QO component [2]. . . . .	10
3.1	A large format flat FPA based on lens antennas with a hybrid architecture. The yellow, green, and orange regions represent the identical, displaced, and enlarged elements regions, respectively. . . . .	12
3.2	CONSORTIS system CAD model [3]. . . . .	13
3.3	CFO spectrum for three typical elements. . . . .	14
4.1	The prototype of the leaky waveguide antenna and zoom-in three-view. . . . .	16
4.2	Main parameter of the doubles slot iris. . . . .	16
4.3	Gaussicity of different cases with a silicon lens and the stratification of such model. . . . .	18
4.4	Simulation result for silicon lens. . . . .	18
4.5	Gaussicity of different cases with an HDPE lens $\epsilon_{r2} = 2.3$ . . . . .	19
4.6	Simulation result for HDPE lens. . . . .	20
4.7	Matching efficiency and phase centre as a function of permittivity of the cavity when scanning broadside in the H(first panel)/D(second panel)/E(third panel) plane. . . . .	21
4.8	Matching efficiency and phase centre as a function of permittivity of the cavity when scanning 24 beams in the H(first panel)/D(second panel)/E(third panel) plane. . . . .	22
4.9	Matching efficiency and phase centre as a function of permittivity of the cavity when scanning 50 beams in the H(first panel)/D(second panel)/E(third panel) plane. . . . .	22
4.10	The parametric study of the the distance between the slots, the permittivity and the thickness of the cavity for the lens scanning 50 beams. . . . .	24
5.1	The top view of lens scanning 50 beams by MATLAB, GRASP and CST. . . . .	28
5.2	Focal plane array of lenses in topview. . . . .	29
5.3	The front, top and side view of the lens located at the 50-beam scanning point. . . . .	30
5.4	The illustration of the QO system with the details of the four regions. . . . .	31

6.1	Radiation pattern and phase performance of the element scanning broad-side. . . . .	34
6.2	Radiation pattern and phase performance of the element scanning 24 beams. . . . .	35
6.3	Radiation pattern and phase performance of the element scanning 50 beams. . . . .	35
6.4	Magnitude and phase of the secondary field. . . . .	36
6.5	Simulation result for magnitude(left two panels) and phase(right two panels) of the secondary field in the H plane and the E plane illuminated by the lens scanning 50 beams by CST MS and in-house PO analysis. (a) the lens with a waveguide feeder at the lower foci; (b) the lens with a displaced waveguide feeder; (c) the lens with a shaped surface; (d) the lens with a matching layer. . . . .	37
6.6	Simulation result for the magnitude of the primary field illuminated by the lens scanning 50 beams by GRASP in the near field (left panel), in the far field (middle panel) and by CST MS in the far field (right panel). (a) the lens with a waveguide feeder at the foci; (b) the lens with a displaced waveguide feeder; (c) the lens with a shaped surface; (d) the lens with a matching layer. . . . .	39
6.7	Simulation result for the magnitude of the reflector far field illuminated by the lens scanning 50 beams by GRASP in the near field (left panel), in the far field (middle panel) and by CST MS in the far field (right panel). (a) the lens with a waveguide feeder at the foci; (b) the lens with a displaced waveguide feeder; (c) the lens with a shaped surface; (d) the lens with a matching layer. . . . .	40

# LIST OF TABLES

3.1	Gaussian beam waist requirement and scan loss of three typical lenses. . .	14
4.1	The optimal geometry of leaky wave antennas. . . . .	23
4.2	Relative permittivity of the cavity of the leaky wave antenna. . . . .	24
4.3	The final design of leaky wave antennas. . . . .	25
5.1	The size and the position of example lenses in the illustration. . . . .	29
6.1	Performance of the lens scanning 50 beams in different cases. . . . .	41



# 1

## INTRODUCTION

### 1.1. APPLICATION: IMAGING RADARS AT 340GHZ

Nowadays, millimetre wave and sub-millimetre wave systems are widely used and developed in many fields. For example, it can be used as an imaging radar in security screening [4–7], where it can detect concealed threats from stand-off distances of several to a few tens of meters [8–12], biomedical imaging [13, 14], through-wall imaging [15, 16] Also it plays an essential role in non-destructive testing [17, 18], astronomy, earth science, and plasma diagnostics [19], range/Doppler mapping of small-particle targets, stand-off Doppler vibrometry or micro-Doppler signature detection and ultra bandwidth communication [20].

Compared with electromagnetic systems operating on other frequencies, millimetre wave and sub-millimetre wave systems have huge absolute bandwidths, short wavelengths, high signal-to-noise detection and tiny changes in target velocity [20], which lead to higher angle resolution, high spatial resolution, relatively small sized antennas [21]. Moreover, one can also benefit from its non-ionising radiation and the ability to operate in all-weather conditions [22].

Simultaneously, there are also significant challenges to these systems. The most serious one is the lack of mature component technology available at these frequencies [22]. Besides, the components are relatively expensive with tighter mechanical tolerances. In a practical application environment, strong atmospheric attenuation can also be a significant problem [20]. Nonetheless, a general decrease in penetration with the increase of the operation frequency and scattering effects due to barrier materials [8] should also be considered.

Such a system requires simplification of the hardware architecture, low-cost and real-time imaging capabilities [22] and high volumetric resolution acquired from a wide field of view at long range [12]. One essential parameter in the design of an imaging radar system is the field of view (FoV). Beam aberrations caused by an optical route length

inaccuracy limit the field of view, while the aerial scans compromise the imaging system's resolution [23]. In this work, we are focusing on security imaging applications and enlarging the FoV of an existing system [24].

The choice of operating frequency has been settled according to the atmospheric windows which are in the regions of 340, 670 and 850 GHz in which the clear air attenuation is locally minimum [12]. Currently, there are several systems operating at 340 GHz as follows: the 340 GHz radar developed by National Aeronautics and Space Administration (NASA) Jet Propulsion Laboratory (JPL) [9, 20, 22, 25, 26], the 340 GHz 3D imaging radar by Concealed Objects Stand-off Real-Time Imaging for Security (CONSORTIS) [27, 28], the 340 GHz imaging radar systems with few-cm range and cross-range resolution developed by Pacific Northwest National Laboratory and the University of St. Andrews [9, 10, 12, 29]. In this project, we also choose 340 GHz as the operating frequency. Therefore, a lens antenna system is chosen as the candidate for the focal plane array of the imager due to flexibility in controlling the radiation pattern via shaping the lens surface.

In this project, we will discuss how to design an optimal lens element in a large format focal plane array (FPA). To evaluate such a large array, a full-wave electromagnetic analysis, including the coupling between the quasi-optical (QO) system and the detector arrays is time-consuming and numerically cumbersome. Therefore, an analytical spectral model is used for accurately and efficiently analysing the coupling by using Fourier optics (FO) [30]. Specifically, Coherent Fourier Optics (CFO) method is applied here, which extends the analysing capabilities to the coupling between multiple QO components. The detailed and clear derivation of FO and CFO are elaborated in [30–32], respectively. Furthermore, to optimise the performance of this large format lens based FPA, a field matching technique is employed between the CFO spectrum and the far field radiated by the antenna feeder inside each lens.

However, in this scenario, one of the problems is that the CFO spectrum is unique for every element in a large array. Therefore, one needs to design antenna elements individually to match their far field to their corresponding the CFO spectrum in each region of the FPA. In addition, the CFO spectrum, for the elements far away from the centre of the array, is asymmetric in the two main planes. To achieve high performance, the desired feeds should also radiate asymmetrically in azimuth angles in the far field [32].

In such scenarios, a standard and widely used design technique is to use Gaussian beam as the test feed of the QO system [3, 24, 33, 34]. In this project, we will also use the Gaussian beam as a reference for the first-order design. Afterwards, single-layer leaky waveguide antennas are considered as the feeders for the final design. As presented in [35], by changing the slot shape and the stratification on top of it, we can shape the pattern radiated by these leaky wave feeders to match the CFO incident field.

After matching the CFO spectrum in amplitude, phase matching is also considered in this project. The phase term is not negligible for the elements far away from the centre of the array. To counteract its effect, the surface of the lens should be reshaped according to the phase term. Following the method mentioned in [32], Zernike expansion is applied in this scenario to construct a new lens surface in order to reduce the effect of phase mismatching.

This project employs the leaky wave antenna design method in [36] to match the spectral fields described in [32]. In [36], the optimal designs for two cases of single-layer configuration with High Density Polyethylene (HDPE) or silicon top are stated. These designs achieved high aperture efficiency in a wide frequency range. We will use the results from this paper as the reference starting point of my project.

## 1.2. GOAL: STUDY THE PERFORMANCE OF A LENS FOCAL PLANE ARRAY ARCHITECTURE WITH LW FEEDS

The aim of this thesis is to design a series of lens antennas used in a large format focal plane array as shown in Fig. 1.1 using the methodology known as Coherent Fourier Optics. The objectives of this thesis are as follows:

- Analyse the Gaussicity of the far field radiated by the leaky wave antenna in Chapter 4.
- Shape the pattern of the leaky wave antenna by modifying the geometry of its double slot iris and the resonant cavity in Chapter 4.
- Modify the lens surface using Zernike expansion to reduce the scan loss caused by phase mismatch in Chapter 5.
- Validate the design by applying Physical Optics (PO) analysis and analyse the performance of the antennas in Chapter 6.

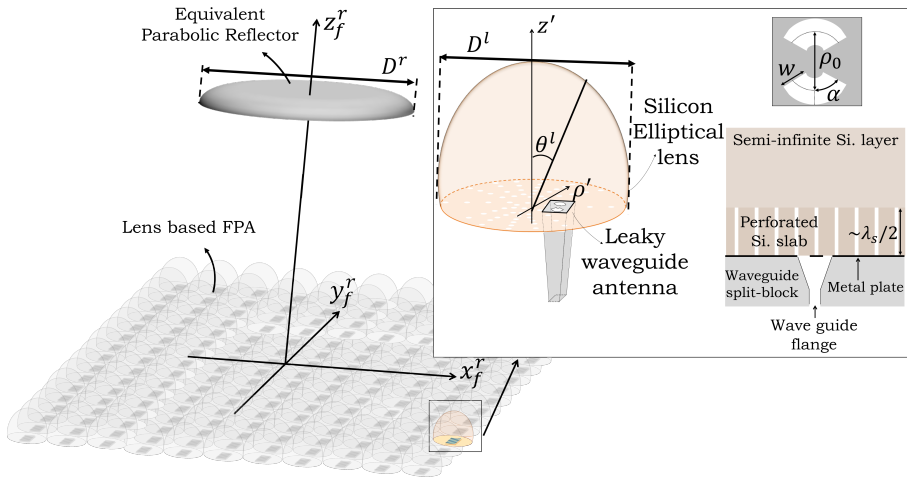


Figure 1.1: An illustration of the large format lens based FPA and the geometry of the leaky wave feeders [1].

## 1.3. GEOMETRY AND PRINCIPLE OF THE LW ANTENNA

In this project, a resonant leaky wave antenna fed by a waveguide is used as the feed of lens elements in the focal plane array, as shown on the right in Fig. 1.1. The double iris antenna and the multi-layer leaky wave antenna are used to shape the pattern of

the feed, avoid the undesired leaky wave mode and enhance the directivity of the lens antenna. In the double iris, the distance between the two slots controls the leaky wave modes and therefore influences the shape of the pattern meanwhile the width and the angle of the slot work for impedance matching of the antenna to the waveguide. The thickness of the multi-layer structure impacts the transmission line model of the antenna which decides the leaky wave mode excited in the structure. The details will be discussed in the following chapters.

# 2

## ARRAY SYNTHESIS METHODOLOGY

### 2.1. ANTENNA IN RECEPTION METHODOLOGY FOR ANALYSING QUASI-OPTICAL SYSTEMS

A QO component is an optical component with dimensions that are modest relative to the wavelength of operation.

Due to reciprocity, a QO system can be analysed either in transmission or reception mode. The analysis in transmission in some cases can be time-consuming because it relies on the Fourier Transform of the equivalent currents transmitted out of the QO components on each rank, known as the equivalent aperture technique. The other option is to analyse the system from the receiving end, which would simplify the calculations. According to the reciprocity theorem, the pattern of the system is consistent whether analysed from the transmission or reception side. Therefore, in this project, we will use reception methodology to design the QO system.

Gaussian beam propagation is a simple and elegant QO analysis technique. The direction of the propagation and variation in the transverse direction is quite clear when the fundamental Gaussian mode is considered. Meanwhile, the Maxwell's equations are simplified, which is known as Paraxial wave equation. It is a rapid method to analyse the system with multiple QO components [2]. In this project, we will shape the feeder pattern to a Gaussian beam to simplify the design.

Note that PO technique is also a well-known way to analyse field radiated by electrically large scatters. Although it is time-consuming, we will use it for final validation.

To optimise the QO system, the aperture efficiency is an essential parameter to be analysed, which is stated as a reaction integral between the frequency independent Geometrical Optics (GO) field on the FO sphere of the QO component and the field radiated by the feeder of such a QO component in an infinite dielectric medium. In the following part, the formula will be derived and these two fields will be evaluated analytically.

Let us start from Thévenin Equivalent Circuit. The power dissipated in a matched load  $P_L$  is calculated from the open circuit voltage  $V_{oc}$ , the amplitude of electric current  $I_{tx}$  illuminating the antenna in transmission and the power  $P_{rad}$  radiated by the antenna excited by the same current amplitude. The equation is shown below [36]:

$$P_L = \frac{|V_{oc} I_{tx}|^2}{16P_{rad}} \quad (2.1)$$

The aperture efficiency is one of the most important parameters for characterising a QO system which indicates how much energy is captured by the matched load from the incident wave by the QO component aperture. According to this definition, the aperture efficiency can be evaluated as:

$$\eta_{ap} = \frac{P_L}{P_{in}} = \eta_{il} \eta_{ref} \quad (2.2)$$

where  $P_{in}$  is the power transmitted from the incident wave by the aperture.

On the other hand, the aperture efficiency is the product of all the factors that affect the performance of a QO component. It mainly includes the illumination efficiency  $\eta_{il}$  and the reflection efficiency  $\eta_{ref}$ . The illumination efficiency consists of taper efficiency and spillover efficiency. And the reflection efficiency indicates how much power is reflected at the air-dielectric interface.

Similar to the steps discussed in [37], we can derive the product of  $V_{oc}$  and  $I_{tx}$  as:

$$V_{oc} I_{tx} \approx \frac{2}{\zeta_d} \int_0^{2\pi} \int_0^{\theta_{edge}} \vec{E}_{GO}^{S_i}(\theta, \phi) \cdot \vec{E}_a^{GP}(\theta, \phi) e^{jk_d \Delta z \cos \theta} dS \quad (2.3)$$

Then the aperture efficiency can be obtained by substituting Eq. 2.1 and Eq. 2.3 into Eq. 2.2 as:

$$\eta_{ap} \approx \frac{|\int_0^{2\pi} \int_0^{\theta_{edge}} \vec{E}_{GO}^{S_i}(\theta, \phi) \cdot \vec{E}_a^{GP}(\theta, \phi) e^{jk_d \Delta z \cos \theta} R^2 \sin \theta d\theta d\phi|^2}{4\zeta_d^2 P_{rad} P_{in}} \quad (2.4)$$

where  $\zeta_d$  is the wave impedance in the lens medium. From Eq. 2.4 we can find that the aperture efficiency will be maximum when the GO incident field  $\vec{E}_{GO}^{S_i}(\theta, \phi)$  and the far field of the antenna  $\vec{E}_a^{GP}(\theta, \phi)$  at the same sphere is conjugated to each other.

## 2.2. COHERENT FOURIER OPTICS: COUPLING OF THE REFLECTOR TO THE LENS BASED FOCAL PLANE ARRAY

Large format detector arrays are transforming millimetre and sub-millimetre imaging systems. FPAs are usually coupled to a QO system with reflectors. For these large QO systems, a full-wave electromagnetic analysis is laborious and time-consuming. Therefore, we will discuss a spectral technique based on Fourier Optics to analyse such a system, so called Coherent Fourier Optics technique [2].

Compared with the CFO technique, the original FO approach is only suitable for a single element QO system coupled to an array of bare absorbers or antennas close to its focal point. Besides, the quadratic phase term is neglected because of the use the incoherent detectors. However, once the coupling between two QO components needs to be analysed, particularly in off-focuses cases, this quadratic phase term can no longer be simplified [2]. To analyse the coupling of the QO system, the lens based FPA and the antennas without missing the phase information, the CFO method will be used to represent the coupling quickly and accurately.

In this project, the plane wave spectrum (PWS) is employed to derive the power captured by the antenna, which is coupled with the lens by applying the reception methodology. It makes it easier to optimise the antenna feeder because of the maximisation of the power received by the antenna when the field of the feeder matches well with the incident PWS.

Let us discuss the model in [2]. In [2], the PWS representation for a QO component illuminated by a plane wave  $\vec{E}^i = E_0 \hat{p} e^{-j\vec{k}^i \vec{r}}$  is in terms of both magnitude and phase of the focal field, where  $\vec{k}^i$  is the wave-vector. In our case, the quadratic phase term is not negligible for representing the coupling between multiple QO components accurately. The spatial field can be represented as:

$$\vec{e}_{f,r}(\vec{\rho}_f) = \frac{1}{4\pi^2} \phi(\vec{\rho}_f) FT^{-1}\{\vec{E}^{FO}(-\vec{k}_\rho)\} \quad (2.5)$$

where  $\phi(\vec{\rho}_f) = e^{-jk|\vec{k}_\rho|^2/(2R_{FO})}$  is the quadratic phase term, and  $FT^{-1}\{\vec{E}^{FO}(-\vec{k}_\rho)\}$  is the inverse Fourier transform of spectral field  $\vec{E}^{FO}(-\vec{k}_\rho)$ . The coherent FO spectrum  $\vec{E}^{CFO}(-\vec{k}_\rho)$  can also be used to represent the spatial field as an inverse Fourier transform as:

$$\vec{e}_{f,r}(\vec{\rho}_f) = \frac{1}{4\pi^2} \int_0^{2\pi} \int_0^{+\infty} \vec{E}^{CFO}(-\vec{k}_\rho) e^{j\vec{k}_\rho \cdot \vec{\rho}_f} k \rho dk \rho d\alpha \quad (2.6)$$

The CFO spectrum is defined as the convolution of the Fourier transform of the quadratic phase term and the spectral FO field as follows:

$$\vec{E}^{CFO}(-\vec{k}_\rho) = \Phi(\vec{k}_\rho) * \vec{E}^{FO}(-\vec{k}_\rho) \quad (2.7)$$

where

$$\Phi(\vec{k}_\rho) = \frac{1}{4\pi^2} \frac{2\pi R_{FO}}{k} e^{-j\pi/2} e^{jR_{FO}|\vec{k}_\rho|^2/(2k)} \quad (2.8)$$

Note that the convolution of Eq. 2.7 is time-consuming and complex. It is important to simplify the steps. By limiting the applicable region around a special position in the focal plane, so called the CFO position,  $\vec{\rho}_{CFO}$ , a new reference system is introduced, where  $\vec{\rho}' = \vec{\rho}_f - \vec{\rho}_{CFO}$ . It helps to linearise the phase term as:

$$k \frac{|\vec{\rho}_f|^2}{2R_{FO}} \simeq k \frac{|\vec{\rho}_{CFO}|^2}{2R_{FO}} + k \frac{\vec{\rho}_{CFO} \cdot \vec{\rho}'}{R_{FO}} \quad (2.9)$$

Then the Fourier transform of the quadratic phase term can be given as:

$$\Phi(\vec{k}_\rho) \simeq e^{-\frac{jk|\vec{\rho}_{CFO}|^2}{2R_{FO}}} \delta(-\vec{k}_\rho - \vec{k}_{CFO}) \quad (2.10)$$

Finally, the CFO spectrum is approximated as:

$$\vec{E}^{CFO}(\vec{k}_\rho) \simeq e^{-\frac{jk|\vec{\rho}_{CFO}|^2}{2R_{FO}}} \vec{E}^{FO}(\vec{k}_{CFO} - \vec{k}_\rho) e^{j|\vec{k}_{CFO} - \vec{k}_\rho| \cdot \vec{\rho}_{CFO}} \quad (2.11)$$

The region of the CFO region is limited where a maximum phase term of the quadratic phase term is  $\pi/8$ :

$$D_{CFO}^{max} = \sqrt{\frac{Df_{\#}\lambda_0}{2}} \quad (2.12)$$

Therefore, the secondary component can be easily coupled to the primary QO component in the region defined by Eq. 2.12. The GO field on the FO sphere of the secondary QO component  $\vec{E}_{sec}^{GO}(\vec{k}_\rho, sec)$  can be calculated as the summation of the contribution of all PWS spectrums in Eq.2.11 coming from the primary QO component.

Besides, the standard FO applicability region can also be expanded in the z-axis. This 3D applicability region defines a region where the coupling between QO components can be approximated by diffraction phenomena, and secondary QO components can be analysed using FO [2].

### 2.3. SPECTRAL GREEN'S FUNCTION: RADIATION PATTERN OF LEAKY WAVE FEEDERS

As mentioned in Section 1.2, a resonant leaky wave antenna is used in this project, the illustration and the transmission line model of the stratification are shown in Fig. 2.1. This transmission line model represents the spectral Green's Function (GF) of the stratification. Based on this GF, the leaky wave modes excited in the structure can be identified

and studied similarly to [38]. In this project, we consider two cases: one is a single-layer configuration as shown in Fig. 2.1a, the other is a double-layer configuration as shown in Fig. 2.1b. The far field radiated by such an antenna can be given by

$$\vec{E}^{far}(\vec{r}) = j k_{zs} \tilde{\mathbf{G}}^{em}(k_{xs}, k_{ys}, z, z') \vec{\mathbf{M}}_{eq}(k_{xs}, k_{ys}) e^{jk_{zs}|z|} \frac{e^{-jk_r r}}{2\pi r} \quad (2.13)$$

where

$k_{xs}$ ,  $k_{ys}$  and  $k_{zs}$  are the projection of the propagation constant on x-, y- and z-axis in the medium,

$\tilde{\mathbf{G}}^{em}$  is Spectral Green's Function which depends on the transmission line shown in the figure below,

$\vec{\mathbf{M}}_{eq}$  is the Fourier Transform of the current.

$$\tilde{\mathbf{G}}^{em} = \begin{bmatrix} \frac{(v_{TM} - v_{TE})k_x k_y}{k_p^2} & -\frac{v_{TM}k_x^2 + v_{TE}k_y^2}{k_p^2} \\ \frac{v_{TE}k_x^2 + v_{TM}k_y^2}{k_p^2} & \frac{(v_{TE} - v_{TM})k_x k_y}{k_p^2} \\ -\frac{\zeta k_y i_{TM}}{k} & \frac{\zeta k_x i_{TM}}{k} \end{bmatrix} \quad (2.14)$$

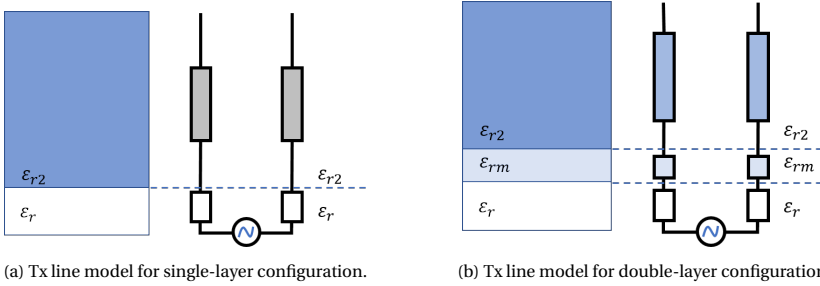


Figure 2.1: Transmission line model.

### 2.3.1. SINGLE-LAYER MODEL

The single-layer one is a leaky wave antenna with a half-wavelength cavity layer filled with tunable material and a semi-infinite layer above. The permittivity of the cavity layer is  $\epsilon_r$  which is the main parameter to be considered. The thickness of such a layer depends on the permittivity as  $h_c = \frac{\lambda_0}{2\sqrt{\epsilon_r}}$  where  $\lambda_0$  is the wavelength in free space.

### 2.3.2. DOUBLE-LAYER MODEL

The double-layer model is an extension of a single-layer model, which contains a quarter-wavelength transformer layer between the cavity layer and the semi-infinite layer. The thickness of the layer is  $h_m = \frac{\lambda_0}{4\sqrt{\epsilon_{rm}}}$  where  $\epsilon_{rm}$  is the permittivity of the slab.

## 2.4. IMPROVING THE SCAN LOSS PERFORMANCE OF A QO SYSTEM VIA PHASE MATCHING IN RECEPTION

Scan loss represents the loss in gain of a multi-beam QO system, which is defined as:

$$SL_{dB}(N_b^s) = -10 \log_{10} \left[ \frac{P_L(N_b^s)}{\max\{P_L(N_b^s)\}} \right] \quad (2.15)$$

where  $N_b^s = \theta^i / (D_r / \lambda_0)$  is the number of beams scanned by the reflector, and  $\theta^i$  is the angle of the incident plane wave illuminating the reflector;  $P_L$  is the power received by the antenna; and  $\max\{P_L(N_b^s)\}$  is the maximum power received by the antenna when the reflector is pointing at broadside direction.

The result of scan loss of an example case is shown in Fig. 2.2. In this example case, provided from [2], the scan loss of a multi-beam QO system is improved by compensating the higher order phase terms for large scanning angles. There are four regions in the figure representing the identical, displaced, enlarged and shaped lenses, respectively. In the next chapter, these four regions will be introduced in detail.

The solid grey line represents the scan loss of the incident focal field. The circle mark near it is the maximum number of beams scanned  $N_b^s = \theta^i / (D_r / \lambda_0)$  where the scan loss is less than 3dB. Note that the result of the incident scan loss curve matches the standard formulas, which is consistent with approximations in the literature. The solid black line shows the scan loss of the array of a homogeneous lens with identical centred feeders. The 3dB scan loss appears when the reflector scans 23 beams. The quick decline of the scan loss is mostly caused by the phase mismatch between the CFO spectrum and the antenna far field because of the quadratic phase term. Moreover, the solid blue line displays the optimal lens based FPA. As shown in the figure, the scan loss for a non-homogeneous lens array is much lower than that when using homogeneous lenses.

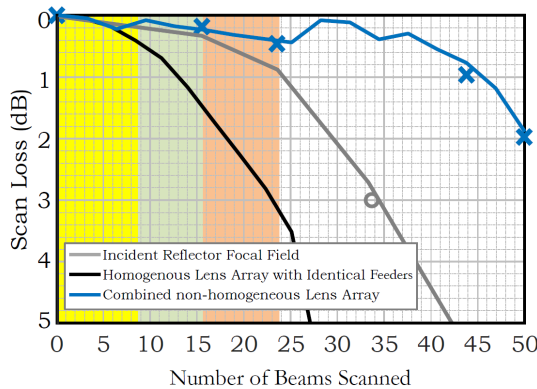


Figure 2.2: Scan loss of the QO system versus the number of beams scanned by the primary QO component [2].

# 3

## CFO DESIGN OF THE FOCAL PLANE ARRAY WITH SHAPED LENS SURFACES

### 3.1. CFO WITH A GAUSSIAN FEED: DESCRIPTION OF THREE REGIONS IN A LARGE FORMAT FOCAL PLANE ARRAY

It is common knowledge that reflector antennas have limited scanning capabilities at large off-broadside angles. In [39–41], the feed clusters are used to enhance the field of view at low frequencies. However, in this thesis, another technique about the design of lens based feeder is considered to enlarge the field of view for a higher frequency band. This solution includes designs for lens dimension, lens surfaces and lens feeders that can be applied to focal plane arrays composed of non-homogeneous elements laying out flatly to provide a monolithic integration.

#### 3.1.1. REGION 1: HOMOGENEOUS LENS ARRAY WITH IDENTICAL FEEDERS

For lens elements around the centre of the focal plane array, the diameter of the lenses is kept at a standard sampling rate of  $D_l = 2\lambda_0 f_{\#,r}$  where  $\lambda_0$  is the wavelength at the centre of the operation frequency band in free space and  $f_{\#,r}$  is the reflector's focal length to the diameter ratio. These elements point to the broadside direction in this region, which is called the centre FO validity region marked in yellow in Fig. 3.1. In this region, we can achieve a high match between the CFO spectrum at the lens FO sphere and the far field of the lens feeder. Therefore, the aperture efficiency for the elements in this region can reach about 80%. As phase mismatch is the primary cause of scan loss, the edge of this region can be defined by the quadratic phase difference over a lens surface

as  $|\Phi_A^q - \Phi_B^q| = \left| \frac{k_0 |\rho_A|^2}{2R_{FO,r}} - \frac{k_0 |\rho_B|^2}{2R_{FO,r}} \right|$  assuming a maximum phase error of  $\pi/2$ . Thus, the

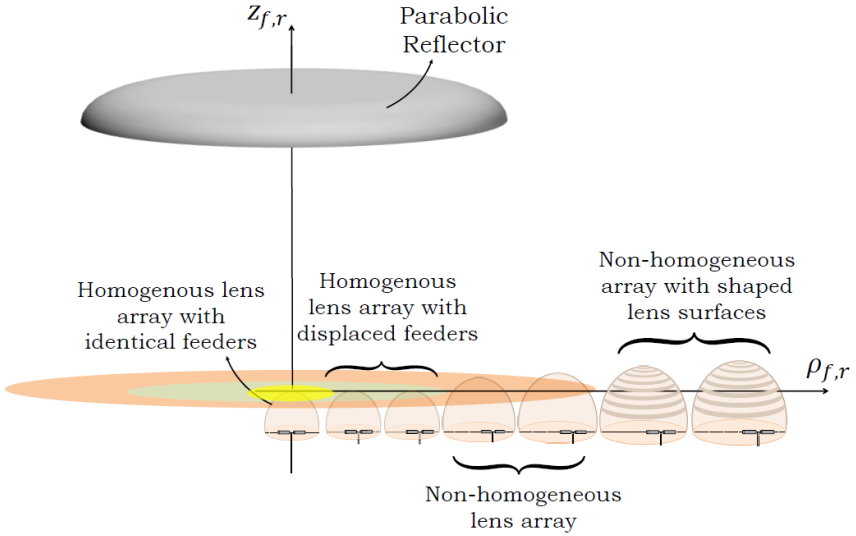


Figure 3.1: A large format flat FPA based on lens antennas with a hybrid architecture. The yellow, green, and orange regions represent the identical, displaced, and enlarged elements regions, respectively.

maximum number of the beam scanning centre FO validity region can be defined as:

$$N_{max}^1 = \frac{\rho_{max}}{\lambda_0 f_{\#,r}} = \frac{D_r}{8\lambda_0 f_{\#,r}} \quad (3.1)$$

### 3.1.2. REGION 2: HOMOGENEOUS LENS ARRAY WITH DISPLACED FEEDERS

For elements in the green area, as shown in Fig. 3.1, the diameter of the lenses keeps the same as that in the yellow area. However, the CFO spectrum shows a linear phase. As a result, the lens feeder needs to be displaced to make its far field conjugate match the CFO spectrum. The position of the lens feeder is defined in [2]. By shifting the feeder, the CFO spectrum and the antenna far field exhibit a good match so that aperture efficiency of 76% can still be achieved. The maximum number of beams scanned can be calculated as the same method in the previous section as:

$$N_{max}^2 = \left[ f_{\#,r} + \sqrt{f_{\#,r}^2 - 0.25} \right]^2 \quad (3.2)$$

### 3.1.3. REGION 3: NON-HOMOGENEOUS LENS ARRAY

For elements farther away in the orange area, the effects of phase mismatch can no longer be offset only by moving the feeder. Therefore, here we need to consider other options. In this region onwards, the CFO spectrum becomes asymmetrical, the main lobe becomes wider, and the edge field taper level becomes lower. To cope with this, an

increase in the diameter of the lens is proposed, the detailed dimensions of which can be found in [2]. The maximum scanned beam number in this region is as follows:

$$N_{max}^3 = 3.15 \sqrt{\frac{D_r}{\lambda_0} \frac{\sqrt[3]{f_{\#,r}}}{2}} \tag{3.3}$$

**3.1.4. REGION 4: NON-HOMOGENEOUS ARRAY WITH SHAPED LENS SURFACE**

As the distance between the lens and the centre of the focal plane increases, the CFO spectrum can no longer be matched to the non-symmetric Gaussian beam. Moreover, this will result in a 5dB loss of scan that cannot be ignored. By improving the phase distribution of the lens, this scan loss can be reduced significantly. By changing the shape of the lens surface, we can change the distance the electromagnetic wave travels through the lens and thus its phase distribution. A more detailed discussion will be developed in the following chapters.

**3.2. APPLICATION CASE: LARGE FORMAT FPA IN AN IMAGING RADAR AT 340GHZ**

Here we consider the application scenario of a state-of-the-art imaging radar, CONSORTIS, discussed in [3] as shown in Fig. 3.2. FPA of the imager is based on horn feeders with an equivalent aperture of  $141.4\lambda_0$  leading to a maximum directivity of 53dBi. However, due to the low capability of horn feeders in shaping the pattern of the system, such a system suffers from a scan loss of 3dB at  $14^\circ$ . Starting from this application case, we will investigate the possibility of enlarging the FoV of such a system using a lens based FPA.

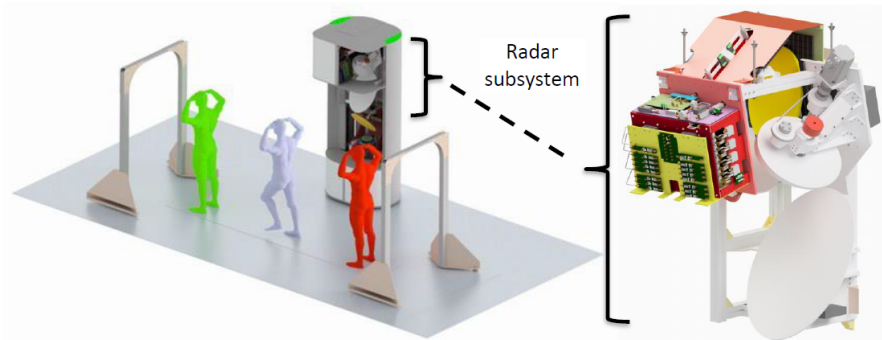


Figure 3.2: CONSORTIS system CAD model [3].

### 3.3. MODELLING THE ANTENNA FEEDER INSIDE EACH LENS ELEMENT AS A GAUSSIAN FEED

Due to the large number of elements in the whole focal plane array, it would be very cumbersome to illustrate each one of them. We can choose one example in each area for our design. For this project, we have chosen to scan broadside, 24 beams and 50 beams for three particular points to study. They are located in the centre of Region 1, the edge of Region 3 and Region 4, respectively. The CFO spectrum of each element is shown in Fig. 3.3. We can find the requirement of Gaussian beam waist and scan loss at each scanning case resorting to the described field matching technique in [2] as shown in Tab. 3.1. The standard deviation of our considered Gaussian far field profiles in the two main planes,  $u_0$  and  $v_0$  are chosen in such a way that the antenna far field matches the CFO at -11dB level.

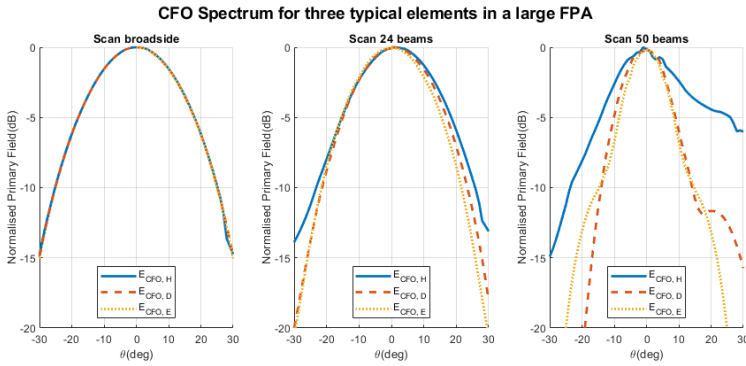


Figure 3.3: CFO spectrum for three typical elements.

Position	Gaussian beam waist		Scan loss	
	$u_0$	$v_0$	Homogeneous	Non-homogeneous
Scanning broadside	0.405	0.405	0	0
Scanning 24 beams	0.405	0.350	3.2dB	0.4dB
Scanning 50 beams	0.3481	0.2197	>5dB	2dB

Table 3.1: Gaussian beam waist requirement and scan loss of three typical lenses.

# 4

## SYNTHESISING THE PATTERN OF THE LEAKY WAVE FEEDER

### 4.1. LENS FEEDER GEOMETRY

In this chapter, we will discuss the design of the lens feeder, which includes a set of double slot iris and resonant leaky wave antenna. The prototype of this antenna is shown in Fig. 4.1a, which is a simplified model of [36]. More details are shown in the three-view in Fig. 4.1b, 4.1c and 4.1d.

Let us start with the double slot iris, whose structure is shown in Fig. 4.2. As we can see in the figures, the double slot iris is fed by a squared waveguide whose size is  $wg = 0.8\lambda_0$  according to the impedance matching at 340GHz. The waveguide works on  $TE_{01}$  mode. The currents of the double slot iris are each defined by Eq. 4.1 and Eq. 4.2. Here we use the numerical result in [36]:

$$\vec{m}_{s1}(\rho, \phi) \approx \frac{1}{\rho} \cos \left[ \frac{\pi}{2\alpha} \left( \phi - \frac{\pi}{2} \right) \right] \text{rect} \left( \phi - \frac{\pi}{2}, 2\alpha \right) \text{rect} \left( \rho - \frac{\rho_0}{2}, w \right) \hat{x} \quad (4.1)$$

$$\vec{m}_{s2}(\rho, \phi) \approx \frac{1}{\rho} \cos \left[ \frac{\pi}{2\alpha} \left( \phi + \frac{\pi}{2} \right) \right] \text{rect} \left( \phi + \frac{\pi}{2}, 2\alpha \right) \text{rect} \left( \rho - \frac{\rho_0}{2}, w \right) \hat{x} \quad (4.2)$$

The distance  $\rho_0$  in the double slot is an essential parameter which influences the illumination efficiency significantly. This is due to its important role in controlling the position of the null in the Fourier Transform of the double slot equivalent currents. As a result, it is used in this work to shape the pattern of the leaky wave antenna. Meanwhile, the width  $w$  of the slot and the angle  $\alpha$  do not play a significant role in pattern shaping but in impedance matching. So we will keep them constant to focus on the optimisation of

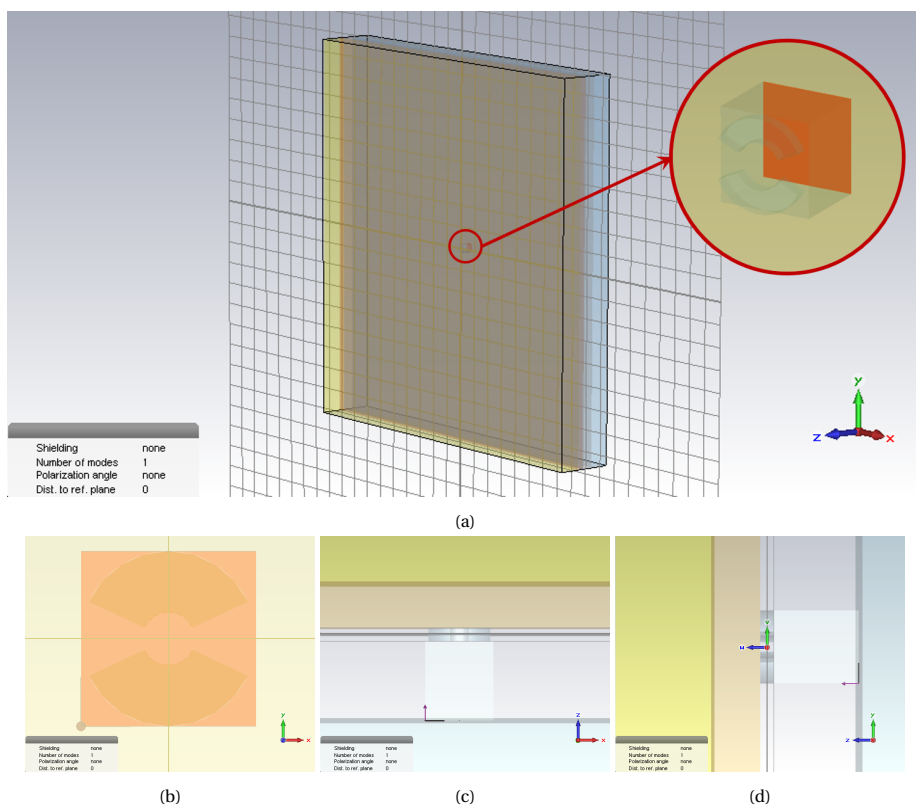


Figure 4.1: The prototype of the leaky waveguide antenna and zoom-in three-view.

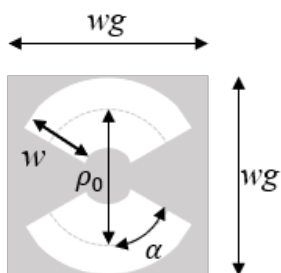


Figure 4.2: Main parameter of the double slot iris.

the design on shaping the pattern while maintaining good impedance match with the waveguide feed.

Then we come to the stratification that excites the leaky wave. There is a cavity between the ground plane and the semi-infinite dielectric medium. In some cases, there is also a quarter wavelength dielectric slab between the cavity and the top as introduced in Section 2.3. By changing the permittivity of the material filling each part, we can shape the far field pattern to what is needed to achieve good field matching performance. The thickness of the cavity and the slab also effect the shape of the pattern. As a result, they are also studied in this project.

## 4.2. FIELD MATCHING TO THE GAUSSIAN BEAM

### 4.2.1. DEFINITION

Gaussicity is a term that describes how well an antenna is coupled to the Gaussian beam as a reference, which is the maximum achievable power coupling of the feed aperture field to a linearly polarised Gaussian beam[42]. If the far field radiated by the target antenna is  $\vec{E}_a$  and the Gaussian beam is  $\vec{E}_g$ , then Gaussicity is given by

$$\eta_{gau} = \frac{|\iint_{\Omega} \vec{E}_a \cdot \vec{E}_g \cdot e^{jk_a \cos\theta \Delta z} \cdot \sin\theta d\theta d\phi|^2}{\iint |\vec{E}_a|^2 \sin\theta d\theta d\phi \cdot \iint |\vec{E}_g|^2 \sin\theta d\theta d\phi} \quad (4.3)$$

where  $k_a$  is the propagation constant in the medium and  $\Delta z$  is the location of the phase centre.

The Gaussian beam for a non-rotationally symmetric case is given by

$$\vec{E}_g = e^{-\left[\left(\frac{u}{u_0}\right)^2 + \left(\frac{v}{v_0}\right)^2\right]} (\sin\phi \hat{\theta} + \cos\phi \hat{\phi}) \quad (4.4)$$

where

$$u = \sin\theta \cos\phi,$$

$$v = \sin\theta \sin\phi,$$

$u_0$  and  $v_0$  are optimised to achieve the highest Gaussicity.

To start with, we can consider a symmetric Gaussian beam which is defined as:

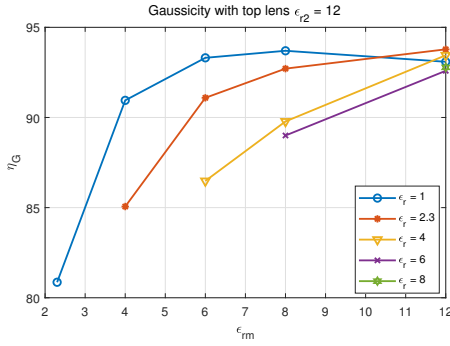
$$\vec{E}_g = e^{-\left(\frac{\theta}{\theta_0}\right)^2} (\sin\phi \hat{\theta} + \cos\phi \hat{\phi}) \quad (4.5)$$

where  $\theta_0$  is optimised to achieve the highest Gaussicity.

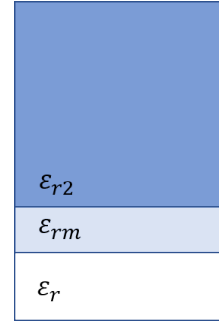
### 4.2.2. CASE 1: SILICON TOP

As discussed in Section 4.1, the pattern can be shaped by modifying the geometry of the leaky wave antenna. Note that if the same material is used in the dielectric slab and the semi-infinite medium, the double-layer configuration is as same as the single-layer one.

At first, we consider a leaky wave antenna with a silicon top. The result is shown in Fig. 4.3a. The cavity is filled with dielectric permittivity  $\epsilon_r$  from 1 to 8 to take advantage of



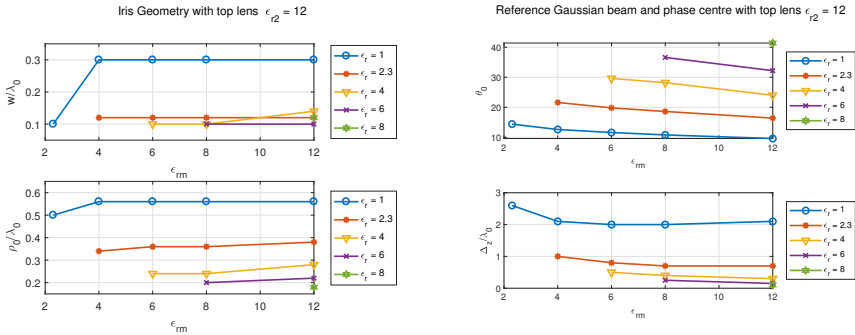
(a) Gaussicity of different cases with a silicon lens  $\epsilon_{r2} = 12$ .



(b) The model for double-layer configuration.

Figure 4.3: Gaussicity of different cases with a silicon lens and the stratification of such model.

the leaky wave. As shown in the figure, Gaussicity increases with the increase of the permittivity of the dielectric slab  $\epsilon_{rm}$  and the decrease of the permittivity of the cavity  $\epsilon_r$ . The Gaussicity of the optimised geometry reaching higher than 90% will be estimated and discussed later. We can find the maximum Gaussicity appears when the dielectric slab is the same as the semi-infinite medium which is silicon and the cavity is filled with HDPE. Therefore, we will focus on the antenna without an extra dielectric slab in the following study.



(a) The geometry of the iris slot of the lens with a silicon top.

(b) The Gaussian waist (first panel) and phase centre (second panel) of the lens with a silicon top.

Figure 4.4: Simulation result for silicon lens.

To reach a high Gaussicity, the iris slot should also be adjusted. Fig. 4.4a shows how the width  $w$  and the distance of the slots  $\rho$  change in different cases. It is obvious that  $\rho$  is unique for each cavity while  $w$  is almost the same for most cases. Therefore, we will pay more attention to how the slots separate during the design.

Gaussicity is calculated by the primary field and the best-matched Gaussian beam. It shows how wide the beamwidth of the primary field is in the first panel of Fig. 4.4b. And the second panel is the phase centre in each case. The larger the permittivity of

the cavity is, the wider the beam is. According to [32], the range of the Gaussian waist is from  $11.53^\circ$  and  $23.57^\circ$ . Therefore, the cases with the cavity permittivity  $\epsilon_r$  from 1 to 4 of single-layer configuration will be considered in the next step. Besides, the phase centre may also influence the final design. With the result in Fig. 4.4b, we can roughly set the permittivity of the cavity as 3 when we consider a lens with a silicon top. The width of the slots is set as  $0.15\lambda_0$ . In this rough estimation, only the amplitude matching efficiency is considered.

### 4.2.3. CASE 2: HDPE TOP

The lens with an HDPE top is estimated by the same steps in Subsection 4.2.2. Compared with the result in Fig. 4.3a, Gaussicity is higher and more constant when the lens is with an HDPE top in Fig. 4.5. The geometry is shown in Fig. 4.6a. It exhibits different characteristics from the silicon top antenna. The Gaussian waist and the phase centre of each case are shown in Fig. 4.6b.

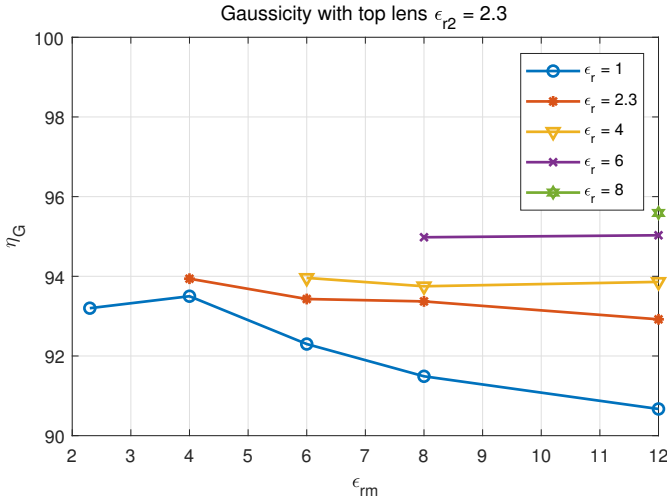


Figure 4.5: Gaussicity of different cases with an HDPE lens  $\epsilon_{r2} = 2.3$ .

In this section, Gaussicity is defined and analysed in two different lens materials fed by the resonant leaky cavity with the double slot iris. We found that when the iris slots are used as the feed, the width of the slot does not influence the radiation pattern much. To shape the pattern, the distance of the slots plays an important role because it will influence the null of the far field which is used to cancel the undesired leaky mode. It is found that the lens with a silicon top and a tunable material inside the half-wavelength cavity as shown in Fig. 2.1a offers the range of Gaussian waist as  $\theta_0 \in [10^\circ, 40^\circ]$  in the single-layer configuration. The lens with an HDPE top offers a wider range of Gaussian waist as  $\theta_0 \in [20^\circ, 60^\circ]$  in the single-layer configuration. We took the design with a silicon top because it is considered easier to be fabricated with the silicon lens and it offers enough range for the CFO spectrum in [32], which requires a tunable Gaussian beam from  $11^\circ$  to  $23^\circ$ . Meanwhile, the Gaussian waist of an HDPE lens is not narrow enough.

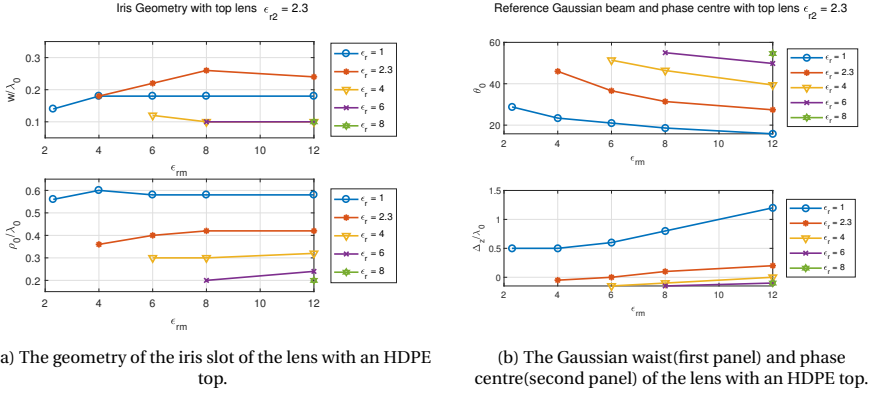


Figure 4.6: Simulation result for HDPE lens.

Therefore, the lens with an HDPE is not suitable for this project.

### 4.3. LEAKY WAVE GEOMETRY

In the previous section, we discussed the Gaussicity of the far field of a leaky wave antenna illuminated by a double iris slot. The reference field is a symmetrical Gaussian beam. However, as shown in Fig. 3.3, for elements further away from the centre of the focal plane, the Gaussian beam is no longer symmetrical. Next, we will discuss the case of a particular plane only. When the reference beam is the CFO incident field, Eq. 4.6 defines a more general efficiency which we call matching efficiency  $\eta_m$  in this project:

$$\eta_{match,1D} = \frac{|\int E_{aco} \cdot E_{match_{ref}} \cdot e^{-j\phi_{match}} \cdot e^{jk_{d2} \cos\theta \Delta z} \cdot \sin\theta d\theta|^2}{\int (|E_{aco}|^2 + |E_{axpol}|^2) \cdot \sin\theta d\theta \cdot \int |E_{match_{ref}}|^2 \cdot \sin\theta d\theta} \quad (4.6)$$

where

$E_{aco}$  and  $E_{axpol}$  are the co-polarised and cross-polarised far field radiated by the antenna in a specific plane,

$E_{match_{ref}}$  is the field that acts as a reference field to calculate the matching efficiency in a specific plane, in this case, the CFO incident field,

$\phi_{match}$  is a possible phase match term,

$k_{d2}$  is the propagation constant in the lens material,

$\Delta z$  is the shift of the phase centre.

#### 4.3.1. CASE 1: SCANNING BROADSIDE

To prevent the optimization process from being stuck in a local maximum, we set a larger sweeping range of the permittivity from 1 to 5. To match the CFO spectrum, the location of the phase centre is also considered.

To simplify the calculation, the matching efficiency is analysed in the H/D/E plane separately. For the lens at the centre of the focal plane which is scanning broadside, matching efficiency between the primary field and the CFO spectrum is shown in Fig. 4.7. It represents the performance of the H/D/E plane from the top to the bottom respectively. To achieve high matching efficiency in every plane, the permittivity should be set from 3 to 4 while the phase centre is  $0.4\lambda_0$  to  $0.6\lambda_0$ .

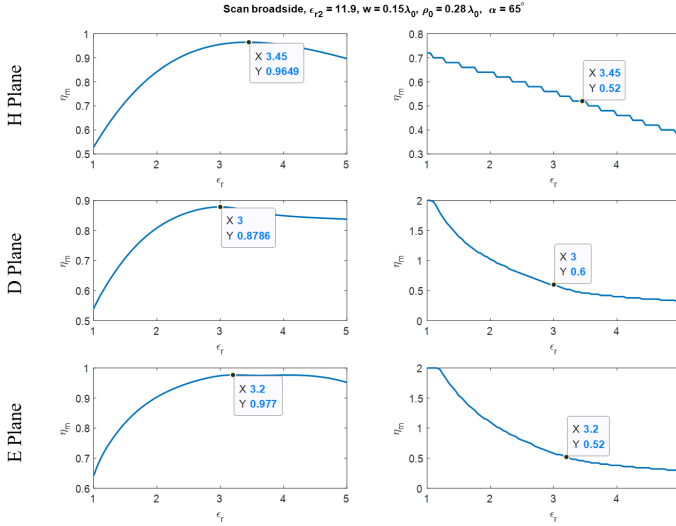


Figure 4.7: Matching efficiency and phase centre as a function of permittivity of the cavity when scanning broadside in the H(first panel)/D(second panel)/E(third panel) plane.

#### 4.3.2. CASE 2: SCANNING 24 BEAMS

For the lens scanning 24 beams, matching efficiency varies more obviously in the E plane, which leads to a smaller range of change of permittivity as shown in Fig. 4.8. Fortunately, it can be seen that the optimal permittivity is still around 3 in three different planes.

#### 4.3.3. CASE 3: SCANNING 50 BEAMS

For the lens scanning 50 beams, the difference on each plane is not negligible any more. As shown in Fig. 4.9, when it performs greatly in the E plane with a cavity of  $\epsilon_r = 1.6$ , the matching efficiency in the H plane is lower than 70%. Similarly, when the permittivity is 3.1, it leads to the best performance in the H plane, while matching efficiency is only 50% in the E plane. Therefore, the permittivity should be rotationally varied in the cavity to reach optimal performance.

In this section, we design the lenses in three specific regions in [32] as scanning broadside, 24 beams and 50 beams. First we find the optimal distance between the slots with a constant width of the slot by a parametric study around the existing prototype in [36].

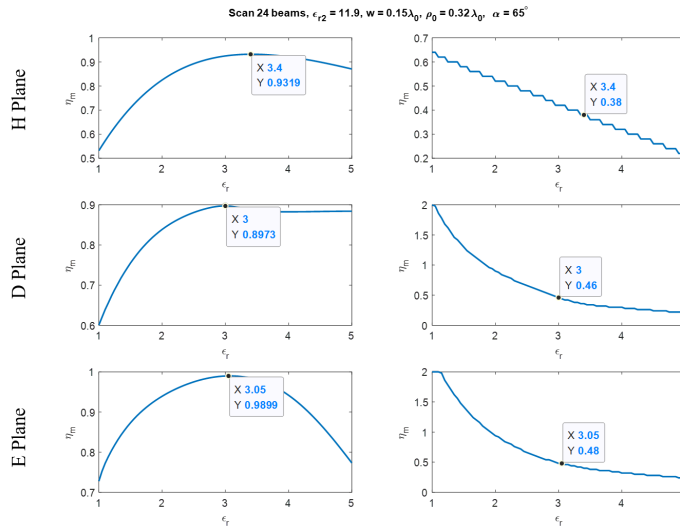


Figure 4.8: Matching efficiency and phase centre as a function of permittivity of the cavity when scanning 24 beams in the H(first panel)/D(second panel)/E(third panel) plane.

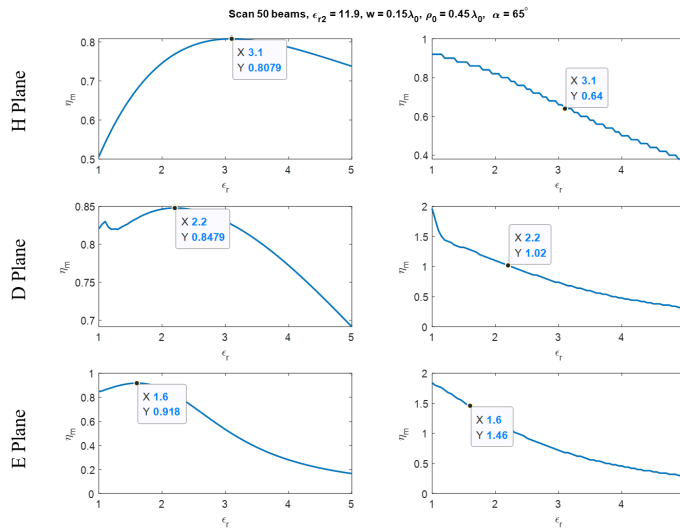


Figure 4.9: Matching efficiency and phase centre as a function of permittivity of the cavity when scanning 50 beams in the H(first panel)/D(second panel)/E(third panel) plane.

The result is then used to find the optimal permittivity in the H/D/E planes to achieve high matching efficiency. According to the design above, the final result is shown in Tab. 4.1 which will be used in the following chapter and validated in CST MICROWAVE STUDIO (CST MS) in Chapter 6.

Element	$\epsilon_{r,cavity}(H/D/E)$	$\rho$	w	$\alpha$
Broadside	3.45/3/3.2	$0.28\lambda_0$	$0.15\lambda_0$	$65^\circ$
24 beams	3.4/3/3.05	$0.32\lambda_0$	$0.15\lambda_0$	$65^\circ$
50 beams	3.1/2.2/1.6	$0.45\lambda_0$	$0.15\lambda_0$	$65^\circ$

Table 4.1: The optimal geometry of leaky wave antennas.

#### 4.4. ASYMMETRIC LEAKY WAVE PATTERNS USING TUNABLE RESONANT CAVITIES

We have already known that the CFO spectrum is not symmetric in the E and H plane when the lens is not in the centre. So we need to have different models in each plane. The ideal resonant cavity should change continuously. However, in a realistic scenario, we will try to use a dielectric cavity with constant permittivity. Therefore, we need to compare the realistic model with the ideal model regarding the matching efficiency.

##### 4.4.1. TRADE OFF DUE TO PERMITTIVITY OF THE CAVITY

Let us first consider the case scanning broadside and 24 beams. According to Fig. 4.7 and Fig. 4.8, we can find the trend of matching efficiency varying with the permittivity of cavity. To simplify the model, the geometry should be as isotropic as possible, both in the effective permittivity of the cavity and the phase centre. The main limitation is that the matching efficiency should be at least 80% in each plane. The results are reported in Tab. 4.2. We can find that the matching efficiency has not been significantly reduced.

As shown in the table, for elements inside the second off-focus FO region, the permittivity and the phase centre can be set as the same for a single lens when the performance is still maintained well. However, for elements in the third off-focus FO region far away from the centre, the relative permittivity of the cavity varies significantly from the E plane to the H plane to match the asymmetrical CFO spectrum. This means the cavity slab can not be as homogeneous as that in other elements. We will discuss how to fabricate such a cavity in the following part.

From Tab. 4.1, we have found that for a lens scanning 50 beams, the optimum values of the permittivity of the material filling the resonant cavity are 3.1, 2.2 and 1.6 in each plane respectively. Then we can perform a parametric study on the permittivity of the cavity  $\epsilon_{rc}$  and  $\rho_0$ . From Fig. 4.10, we can find a peak whose corresponding value can be

Element	Plane	$\epsilon_{r,max}$	$\eta_{m,max}$	$\epsilon_{r,opt}$	$\eta_{m,opt}$	$\eta_{m,opt}/\eta_{m,max}$
Broadside	H	3.45	0.9649	3.2	0.9623	99.7%
	D	3	0.8786	3.2	0.8755	99.6%
	E	3.2	0.9770	3.2	0.9770	100%
24 beams	H	3.4	0.9319	3.05	0.9253	99.3%
	D	3	0.8973	3.05	0.8964	99.9%
	E	3.05	0.9899	3.05	0.9899	100%
50 beams	H	3.1	0.8079	2.55	0.8007	99.1%
	D	2.2	0.8479	2.55	0.8467	99.8%
	E	1.6	0.9180	2.55	0.9084	98.9%

Table 4.2: Relative permittivity of the cavity of the leaky wave antenna.

taken to help us narrow down the range. Next, we do a parametric study on  $\rho_0$  and the resonant cavity thickness  $h_c$ , for different  $\epsilon_{rc}$  values, as shown in Fig. 4.10. Eventually we can find that there is a maximum aperture efficiency when  $\rho_0 = 0.38\lambda_0$ ,  $h_c = 0.26mm$  and  $\epsilon_{rc} = 2.55$ . The matching efficiency in each plane does not decrease a lot as shown in Tab. 4.2 The final design is shown in Tab. 4.3.

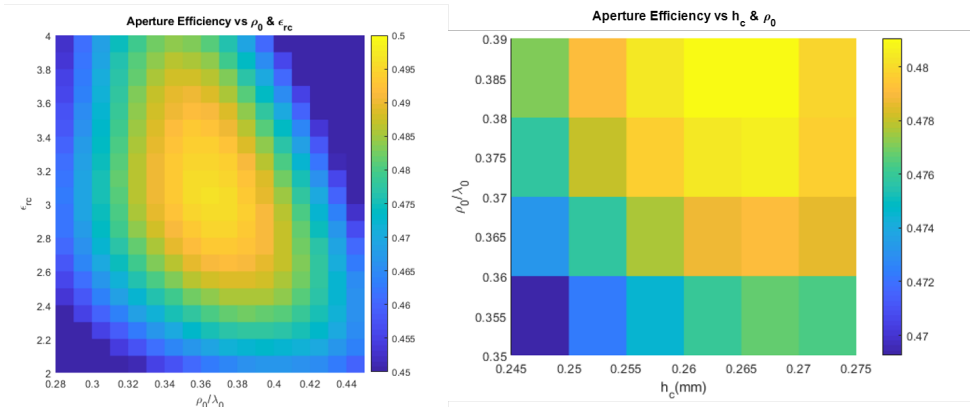


Figure 4.10: The parametric study of the the distance between the slots, the permittivity and the thickness of the cavity for the lens scanning 50 beams.

Element	$\epsilon_{r,cavity}$	$\rho$	w	$\alpha$
Broadside	3.2	$0.28\lambda_0$	$0.15\lambda_0$	$65^\circ$
24 beams	3.05	$0.32\lambda_0$	$0.15\lambda_0$	$65^\circ$
50 beams	2.55	$0.38\lambda_0$	$0.15\lambda_0$	$65^\circ$

Table 4.3: The final design of leaky wave antennas.



# 5

## SYNTHESIS OF THE LARGE FORMAT LENS BASED FOCAL PLANE ARRAY

### 5.1. REPRESENTING THE LENS SURFACE USING THE ZERNIKE EXPANSION

Here we start to create the surface of a non-analytical lens which is located in Region 4 defined in Subsection 3.1.4.

According to [43, 44], the phase difference between the elliptical lens CFO spectrum and the translated non-symmetric Gaussian lens feeder approximately follows Zernike expansion. Following the findings in [2], here we apply the following modification to the surface of an elliptical lens in the vertical direction:

$$d_m(\rho, \phi) = \frac{Z_h(\rho, \phi)}{k_{dz} - k_{0z}} \quad (5.1)$$

where

$d_m$  represents the difference in lens height,

$\rho$  and  $\phi$  denote the position on the lens surface,

$Z_h$  indicates Zernike approximation of the hologram phase,

$k_{dz} = k_d \cos \theta_l$  is the z-component of the propagation constant in the lens material [2].

As a result, the complex phase difference is converted into a simple height difference of the lens surface. The modification can be added onto a standard lens to achieve phase correction. Therefore, the shape of the lens surface can be defined by simply using the matching Zernike expression to obtain the height difference at each location on the lens surface. A Zernike expansion can be represented as [43, 44]:

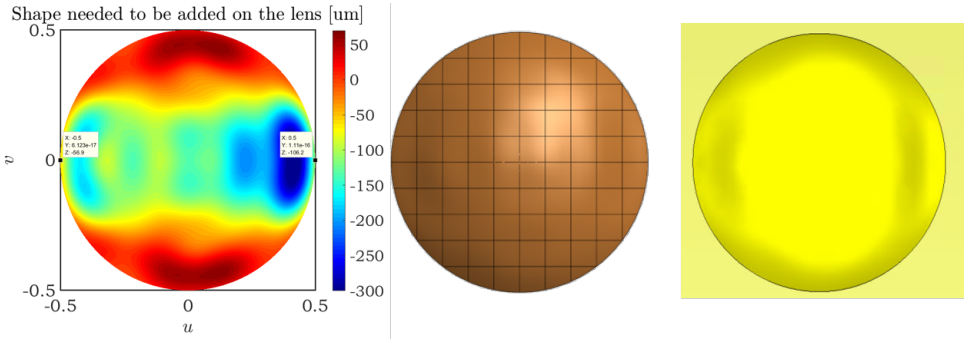


Figure 5.1: The top view of lens scanning 50 beams by MATLAB, GRASP and CST.

5

$$F(\rho, \phi) \approx Z_N^M = \sum_{m=0}^M \sum_{n=0}^N [A_n^m O_n^M(\rho, \phi) + B_n^m E_n^M(\rho, \phi)] \quad (5.2)$$

where  $F(\rho, \phi)$  is an arbitrary function;  $0 \leq \rho \leq 1$  and  $0 \leq \phi \leq 2\pi$  are the usual polar coordinates of an arbitrary point;  $Z_N^M$  is a Zernike polynomial of order  $N$  and  $M$ ;  $O_n^m$  and  $E_n^m$  are the odd and even Zernike polynomials;  $A_n^m$  and  $B_n^m$  are the weight coefficients. In the previous section, we took the example of a lens scanning 50 beams as Region 4, which is located at  $\vec{\rho}_{f,r} = 50\lambda_0 f_{\#,r} \hat{x}$ . The Zernike mode of  $M = 30, N = 30$  is applied in this case. The results of the distance  $d_m$  is shown in Fig. 5.1 in MATLAB, GRASP and CST, respectively.

## 5.2. IMPORTING THE LENS SHAPE TO 3D ELECTROMAGNETIC DESIGN SOFTWARE

Since the Zernike surface cannot be described in a simple analytical form, it was not possible to generate it in a defined form using one single software. Therefore, to create the final 3D presentation, we will use GRASP, CST MS and AutoCAD together.

First, the matrix of height modifications is generated in MATLAB according to the definition of the Zernike expansion in the previous section and exported as a .zer file. This is then imported into GRASP and merged onto a standard lens surface. In this step it is important to note the positive and negative height modifications. Next, the .stp describing the shape of the lens surface can be exported to CST. We can finally obtain a design model of each lens and the entire system by importing the .stp model from CST into AutoCAD and modifying the arrangement.

Following the CST modelling of representative elements, we can turn our attention to the full antenna array and use AutoCAD to create the final rendering. As previously stated, the antenna array can be separated into four regions. All of the lenses in the first three regions are standard elliptical lenses. The fourth region is the only one that includes shaped lenses. As a result, we can use a few specific pieces to create a three-dimensional

schematic model of the antenna array. Please note that we analysed different points for the sake of simplicity and did not consider the antenna array’s overall performance. In actual applications, it is also necessary to carefully evaluate the coupling relationship between the antennas.

As an illustration, we will use seven points along the x-axis as a starting point. The following table depicts the relationship between the radius and the location of the point of interest.

**5.2.1. CHOOSING REPRESENTATIVE POINTS AND GIVING THE LENS SIZE**

Each zone is defined by the distance between the lens’s centre and the antenna array’s centre, as described in Section 3.1. The antenna array is arranged in a two-dimensional rectangular pattern. As a result of some items not being at the intersection of arrays parallel to the x and y axes, the distance between the two centres must be rounded to achieve the corresponding region definition and lens radius. The size and the location of the elements are shown in Tab. 5.1. The focal plane array is shown in Fig. 5.2, where small circles in different colour refer to the lenses with different radii and large circles refer to different regions defined in Section 3.1. The radius R is normalised by the wavelength and f number of the lens.

Number	1	2	3	4	5	6	7
Region	1	1	2	3	4	4	4
$D_{lens}/\lambda_0 f_{\#,r}$	2	2	2	2.1	3.66	4.66	5
$\tilde{\rho}_{f,r}/\lambda_0 f_{\#,r}$	0	8	15.5	23.5	34	43	50

Table 5.1: The size and the position of example lenses in the illustration.

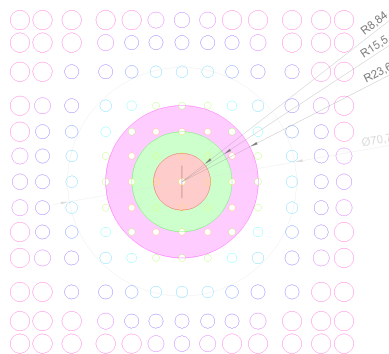


Figure 5.2: Focal plane array of lenses in topview.

### 5.2.2. GENERATING ZERNIKE MATRIX IN MATLAB

Now we have known the equation that represents the correction part. Following the steps in [44] and [2], we can generate Zernike matrix in MATLAB. The weight coefficients  $A_n^m$  and  $B_n^m$  can be represented as a function of the integral of the radial function  $R_n^m(\rho)$ . The Zernike mode is  $M = 30$  and  $N = 30$ . The matrix is printed as a GRASP format to export into another commercial software.

### 5.2.3. IMPORTING .ZER FILES FROM MATLAB INTO GRASP

The generation of shaped lens surfaces in GRASP can be done as follows.

- Importing .zer file.
- Creating a reflector with a metal plane and Zernike matrix.
- Narrowing the reflector rim by the lens size.
- Creating a surface ellipsoid and adding it to the reflector.
- Exporting the reflector by the reflector coordinate system.

### 5.2.4. IMPORTING .STP FILES FROM GRASP INTO CST

The surface morphology of the lens can be obtained in GRASP with the Zernike surface already superimposed, allowing for more precise and realistic simulations in CST. Note that we only acquire an irregular surface with a projection of radius  $D_{lens}$ , which can only support us in the construction of a lens, which must also be filled with the proper material, for example silicon in this model.

### 5.2.5. IMPORTING .STP FILES FROM CST INTO AUTOCAD

The CST model created during the preceding process will be loaded into AutoCAD to create the final schematic, as well as used for future simulation verification. Previously, we concentrated on acquiring the component morphology in Region 4 due to their non-analytical shape. Similarly, during the import into AutoCAD, we can select to assemble the components of the first three zones using an analytical expression or by importing a.stp file. However, we can only choose the latter method in the case of Region 4.



Figure 5.3: The front, top and side view of the lens located at the 50-beam scanning point.

### 5.2.6. ROTATING THE MODEL ACCORDING TO THE POSITION

Since the design of the lens elements mentioned above is based on a coordinate system with the same x- and z- axes as the whole system, when these units are distributed in areas that are not on the x-axis, they need to be rotated to ensure that they remain in the same coordinate system as the incident field at the corresponding position. Here, we do not consider coupling between elements but only rotate them according to their position relative to the centre of the focal plane array. The angle of rotation is the angle between the line of the lens and the centre of the focal plane array and the x-axis of the focal plane array, and the axis of rotation is the z-axis of this lens.

## 5.3. 3D CAD VIEW OF THE ENTIRE FPA WITH THE REFLECTOR

After illustrating the lens elements, as shown in Fig. 5.3, we obtain the three-dimensional schematic diagrams of all the antenna elements and combine them to obtain the schematic diagram of the antenna array.

We can intuitively see the relationship between the respective sizes and positions of the antenna array and reflector in this illustration in Fig. 5.4.

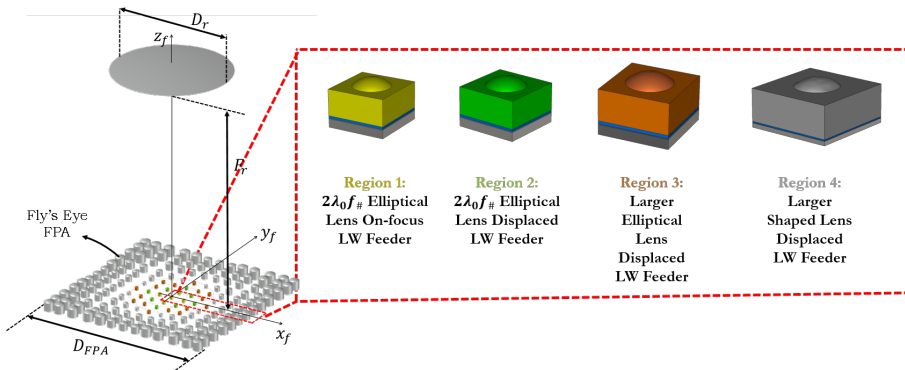


Figure 5.4: The illustration of the QO system with the details of the four regions.

It should be noticed that the phase centres of the lenses at different grid positions are different. As a result, in order to obtain a radiation wave with the same phase, the position of each lens on the z-axis must be modified, which results in a slightly cluttered side view of the antenna array. However, we may neatly encase the lens in a thicker slab. Then, we obtain the three-dimensional schematic diagrams of all the antenna elements and combine them to obtain the schematic diagram of the antenna array. We can intuitively see the relationship between the respective sizes and positions of the antenna array and reflector in this illustration.



# 6

## VALIDATION USING COMMERCIAL SIMULATORS

### 6.1. EVALUATING THE PERFORMANCE OF THE LENS ANTENNA ELEMENTS USING CST

After finding the optimal prototype in MATLAB, we turn to CST MS for full wave simulation to validate our results in Section 4.4. In this chapter, we will implement the simplified model in CST MS and validate the results from MATLAB for three different cases in 6.1.1 to 6.1.3, according to Tab. 4.3.

According to the geometry shown in Tab. 4.1 and Tab. 4.2, the proposed model can be implemented in CST MS. The three views of the feed antenna are shown in Fig. 4.1. To avoid the influence of the reflection at the edge of the configuration, the simulation box is fixed to  $20\lambda_0$  which is more than 30 times as the width of the largest waveguide. The double iris slot is illuminated by a square waveguide of which the width is equal to the outer radius of the iris slot. The length of the waveguide is half wavelength. The thickness of the ground plane is set as  $0.08\lambda_0$ . The background is set with the same permittivity as the top silicon layer.

The results below depict the optimum feed patterns for three different scanning scenarios. The findings produced by utilising the spectral code are also compared to those obtained by using the full wave simulation performed by CST MS. As can be observed, the far field of the designed feeds is well matched with their corresponding the CFO spectrum, and the far field of the designed feeds is consistent with full wave simulations.

#### 6.1.1. CASE 1: SCANNING BROADSIDE

The result of the element scanning broadside is shown in Fig. 6.1. The solid coloured lines are the leaky far field in MATLAB. The dot lines are the simulation in CST. The blue, red and yellow lines represent co-polarised part of the far field in the H/D/E plane,

respectively. The great agreement is shown between the result from MATLAB codes and the results from CST MS simulation in both amplitude and phase dimension. The solid pink lines are the CFO spectrum and the dash black lines are the related Gaussian beam. Besides, in the second panel, there are two lines in purple indicating the cross polarisation of the leaky far field. The aperture efficiency on the FO sphere is 79.9% which is extremely close to the one calculated with a standard Gaussian beam as 80.0% in [2]. Therefore, this can be regarded as a useful prototype for future study,

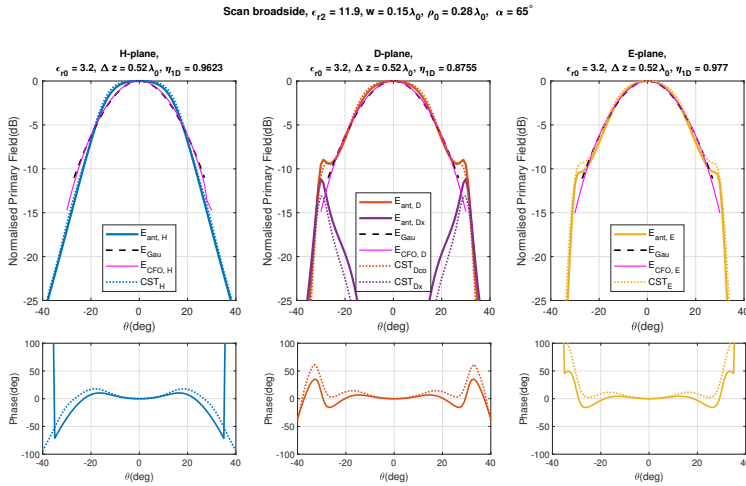


Figure 6.1: Radiation pattern and phase performance of the element scanning broadside.

### 6.1.2. CASE 2: SCANNING 24 BEAMS

For the element scanning 24 beams, the lens antenna is larger and the phase correction term is also working to remove the higher order phase term on the lens CFO. The performance for the prototype is still good, as shown in Fig. 6.2. The primary field in the E plane almost perfectly matches the CFO field. The aperture efficiency on the FO sphere is 72.0% which is well matched with the one calculated with a standard Gaussian beam as 72.8% in [2].

### 6.1.3. CASE 3: SCANNING 50 BEAMS

As shown in Fig. 4.9, the matching efficiency can not reach 85% in the D plane and the H plane because of the asymmetric CFO spectrum in the whole rim, as shown in Fig. 6.3. Fortunately, the matching up to -11dB is still considerable in the E plane which means over 90% of the received power is well-matched. The magnitude of cross-polarised component is also much lower here.

In this section, we validate the design in CST MS. The prototype of the three considered cases is designed in CST MS individually. The simulation results show great agreement between PWS analysis and Full Wave simulation. However, despite the success demon-

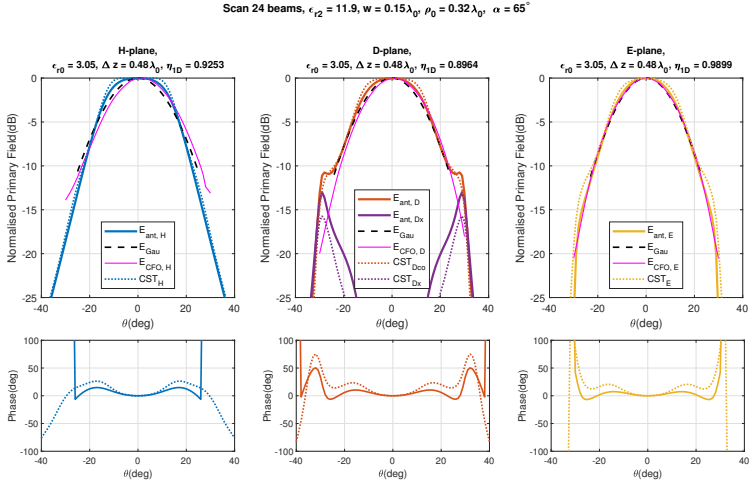


Figure 6.2: Radiation pattern and phase performance of the element scanning 24 beams.

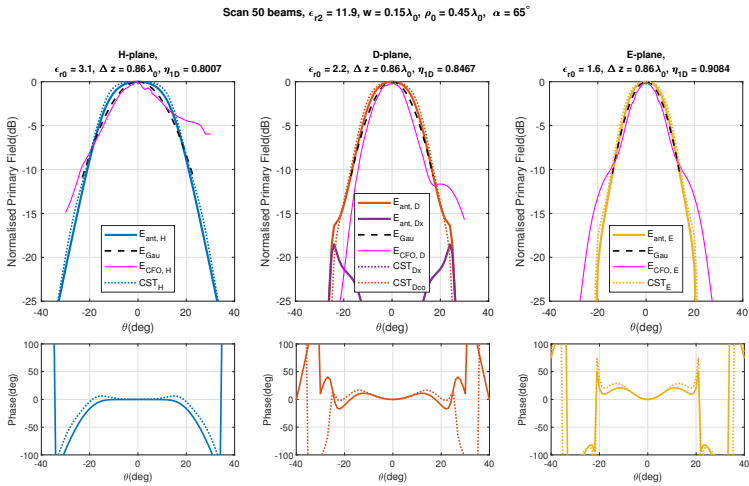


Figure 6.3: Radiation pattern and phase performance of the element scanning 50 beams.

strated, a significant limitation is that for the 50 beam scanning case, the simulation is carried out in three different models to match the asymmetric CFO spectrum. This is addressed in the next subsection.

## 6.2. EVALUATING THE PERFORMANCE OF ONE LENS ANTENNA ELEMENT WITH DISPLACED FEEDER AND SHAPED SURFACE USING CST

In the previous section, for the element scanning 50 beams, we discussed its performance in different planes. However, for more practical situations, an isotropic cavity would be used. As mentioned in Tab. 4.3, we chose its permittivity to be 2.55. In this section, we will discuss the performance of a more realistic lens scanning 50 beams.

In Fig. 6.4, the magnitude and phase of the secondary field are shown in different cases. The standard Gaussian beam is in the first panel. Next is the symmetric Gaussian beam which is an average result. The third and fourth panels illustrate the results of the far field of the lens filled with a cavity of 2.55 with good agreement. The last panel shows the CFO spectrum at the lens FO sphere. From the figures, we can find out how the lens matches the CFO spectrum. In the next subsections, we will look at the effect of the feeder location and lens shape on the compensation of the phase aberrations for 50 beams scanning case and the achieved performance for each case.

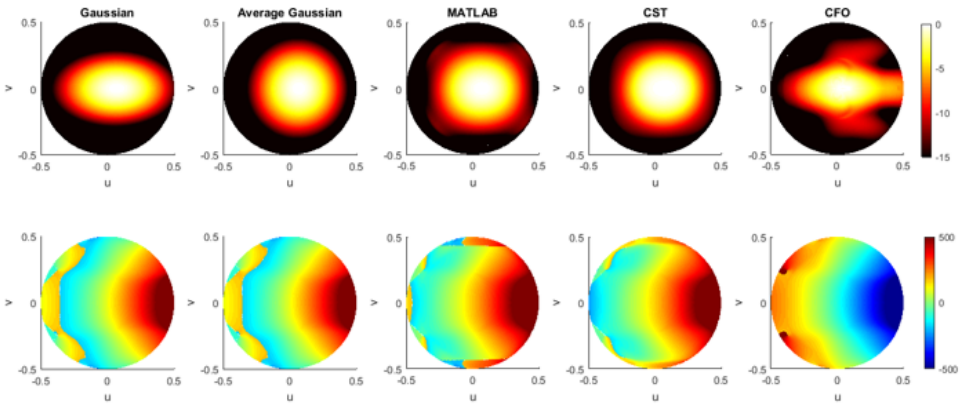


Figure 6.4: Magnitude and phase of the secondary field.

### 6.2.1. FEEDER AT THE FOCUS OF THE LENS

Let us first consider the case when the feeder is at a lower focus. As shown in Fig. 6.5a, the result shows great agreement between CST and PO method. The main beam points to the broadside and the directivity is 27.72dBi by CST MS and 27.74dBi by PO method. The phase centre is at -0.56mm.

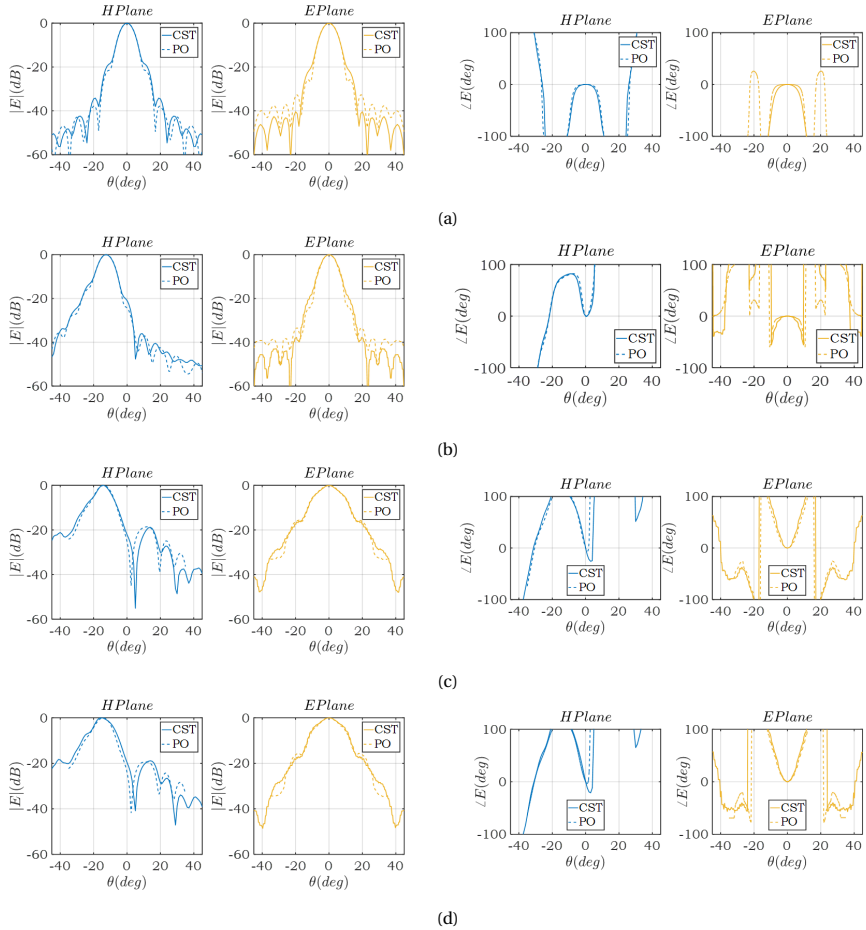


Figure 6.5: Simulation result for magnitude(left two panels) and phase(right two panels) of the secondary field in the H plane and the E plane illuminated by the lens scanning 50 beams by CST MS and in-house PO analysis. (a) the lens with a waveguide feeder at the lower foci; (b) the lens with a displaced waveguide feeder; (c) the lens with a shaped surface; (d) the lens with a matching layer.

### 6.2.2. DISPLACED FEEDER OVER THE LENS FOCAL PLANE

Fig. 6.5b illustrates the far field with a displaced feed. With the displacement of the feeder, the main beam points to  $-13^\circ$  and the directivity is 27.16dBi by CST MS and 27.39dBi by PO method. The translation distance is 0.64mm in the positive direction of the x-axis. The phase centre is at -0.56mm.

### 6.2.3. SHAPED LENS SURFACE WITH AND WITHOUT A MATCHING LAYER

Then the lens surface is shaped by Zernike expansion. As shown in Fig. 6.5c and 6.5d, the main lobe points to  $-14^\circ$ , which is the same as the result of the lens with a matching layer made by Parylene C. The permittivity of the matching layer is 2.95.

In this section, we discussed the design of the lens antenna scanning 50 beams and showed the far field radiated by the lens step by step. In Fig. 6.5, we can simply find the differences between each case. With the displacement of the fed antenna, a linear phase appears. The pattern in the H plane points to the other side meanwhile the pattern in the E plane maintains the same. The pattern is not symmetric now. This will ensure that the reflector is well illuminated in both planes. After adding the shaped top, the phase is then modified further. The pattern becomes wide in each plane to match the incoming field. When covered with the quarter-wavelength matching layer, the radiation does not change significantly. However, the transmission is improved with the matching layer.

## 6.3. EVALUATING THE PERFORMANCE OF THE COMPLETE QO SYSTEM USING CST AND TICRA GRASP

We have already known the performance of the secondary field, next we will evaluate the performance of the whole QO system, presenting the pattern of the final far field, and indicating the direction of the main lobe and directivity. The results are shown in Fig. 6.6, Fig.6.7 and Tab. 6.1.

As can be seen, the displacement of the feeder increases both spill-over efficiency and taper efficiency. The directivity increases by about 2dB. And the addition of Zernike surface reduces the scan loss caused by phase mismatch and increases the antenna gain by about 3dB. Finally, the lens with a shaped surface illuminated a displaced feeder and covered by a Paylene matching layer provides the directivity at about 50dB, pointing to  $20.2^\circ$ .

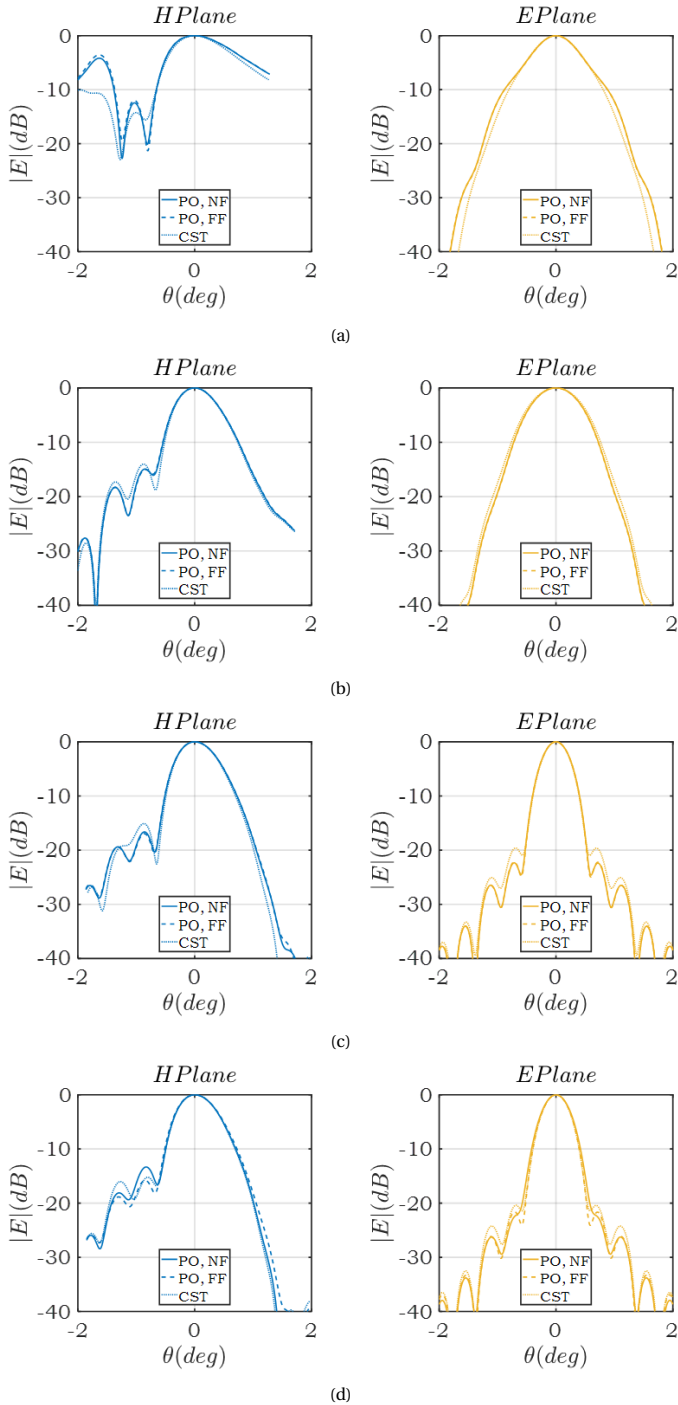


Figure 6.6: Simulation result for the magnitude of the primary field illuminated by the lens scanning 50 beams by GRASP in the near field (left panel), in the far field (middle panel) and by CST MS in the far field (right panel). (a) the lens with a waveguide feeder at the foci; (b) the lens with a displaced waveguide feeder; (c) the lens with a shaped surface; (d) the lens with a matching layer.

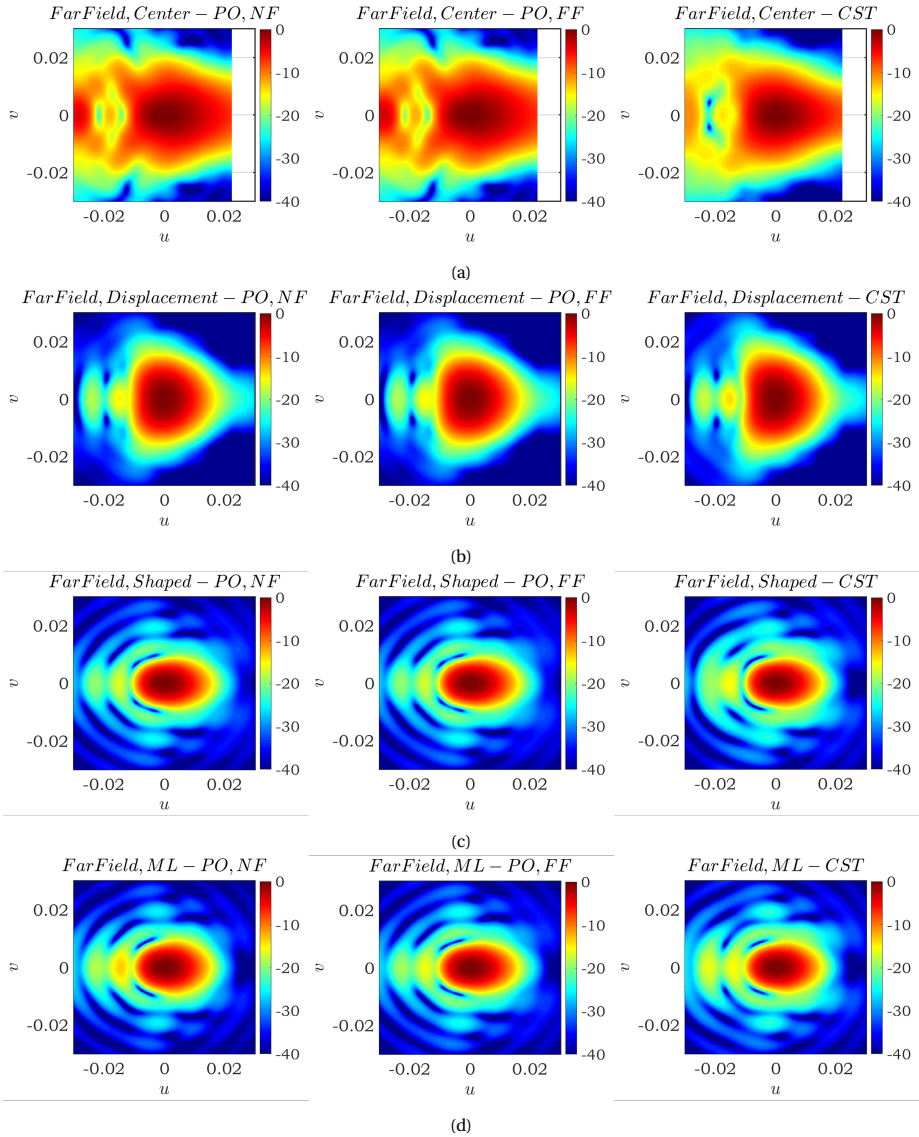


Figure 6.7: Simulation result for the magnitude of the reflector far field illuminated by the lens scanning 50 beams by GRASP in the near field (left panel), in the far field (middle panel) and by CST MS in the far field (right panel). (a) the lens with a waveguide feeder at the foci; (b) the lens with a displaced waveguide feeder; (c) the lens with a shaped surface; (d) the lens with a matching layer.

Case	Efficiency	Far Field( $r = 1 m$ )		Near Field( $r = 0.1 m$ )
		CST	PO	PO
Feeder at the focus	$\eta_s$	0.0255	0.0182	0.0186
	$\eta_t$	0.1649	0.1211	0.1238
	$\eta_{ap}$	0.0037	0.0022	0.0023
	Dir	45.1242	43.7842	43.8774
Displaced feeder		CST	PO	PO
	$\eta_s$	0.9487	0.9535	0.9533
	$\eta_t$	0.2745	0.2885	0.2877
	$\eta_{ap}$	0.2604	0.2751	0.2743
	Dir	47.3376	47.5532	47.5413
Shaped surface		CST	PO	PO
	$\eta_s$	0.8630	0.8830	0.8839
	$\eta_t$	0.5446	0.5288	0.5269
	$\eta_{ap}$	0.4699	0.4669	0.4657
	Dir	50.3125	50.1848	50.1694
Matching layer		CST	PO	PO
	$\eta_s$	0.8552	0.8872	0.8950
	$\eta_t$	0.5397	0.5314	0.5165
	$\eta_{ap}$	0.4616	0.4715	0.4622
	Dir	50.2735	50.2065	50.0824

Table 6.1: Performance of the lens scanning 50 beams in different cases.



# 7

## CONCLUSION

### 7.1. SUMMARY AND CONCLUSION

In this project the design of leaky wave lens antennas in a large format focal plane array for three scanning cases is described. Here the design is achieved using the Coherent Fourier Optics and leaky wave antenna design methods.

In Chapters 2 and 3, we introduced the fundamental theories applied in this thesis. In this work, we used the reception methodology to analyse the QO system according to the reciprocity theorem. The antenna analysis is based on Spectral Green's Function. Moreover, the QO system design applied the Coherent Fourier Optics methodology. The four different regions of this method are also introduced.

In Chapter 4, we studied the leaky wave antenna and got the optimal design. First, we analysed the Gaussicity of silicon-top and HDPE-top leaky wave antennas with a single slab and double slabs and decided to use a silicon lens. These two cases are both illuminated by the double-iris slot. Then the detailed design of the silicon-top antenna in the H, D and E planes is discussed to reach the optimal prototype when scanning broadside, 24 beams and 50 beams. This part of the work is published in [45].

In Chapter 5, we discussed how to model the prototype in commercial software. Here we introduced the steps of surface shaping in MATLAB, GRASP, CST and AutoCAD and finally obtained the optimal shaped lens antenna. The lens surface is shaped by Zernike expansion to achieve better phase matching.

In Chapter 6, the proposed design is implemented in CST to validate the far field obtained from MATLAB with excellent agreement. By importing the secondary field into GRASP, we can finally get the performance of the FPA. The focal plane array based on silicon lenses fed by resonant leaky wave cavities achieves a directivity of 50dB at the edge of the focal plane while scanning  $20.2^\circ$ . The aperture efficiency is about 47%. These results are included in [46].

## 7.2. FUTURE OUTLOOK

Future directions related to the improvement of this work are suggested in the following:

- Frequency analysis. In this thesis, we have only calculated the aperture efficiency of the lens antenna at a centre frequency of 340 GHz but have not performed a frequency analysis of it. In subsequent studies, a frequency analysis should be performed for each lens antenna to characterise its properties.
- Impedance matching. The waveguide mentioned in this study is a rectangular waveguide filled with air and impedance matching is not considered. It can be subsequently replaced with a tapered waveguide filled with other materials to improve the impedance matching efficiency.
- Material optimisation. In [45], it is mentioned that quartz lenses are less expensive to fabricate than plastic lenses and silicon lenses while offering similar scanning performance to plastic lenses and wider bandwidth performance. Next, we can alter the materials to achieve cost-performance trade-offs.
- Fabrication and measurement. In Chapter 5, we have obtained the matrix of the surface of the asymmetric lens. This means that it becomes possible to make a prototype. Next, the model can be measured to verify the design.
- Automated calculation tools. In this study, three canonical cases are developed and discussed to demonstrate the feasibility of the design approach. As a result, the design process can be encapsulated as a MATLAB based Graphical User Interface (GUI). The design of a leaky lens antenna can be output by simply entering the number of scanned beams, the parameters of the parabolic antenna, etc.
- System analysis. Once the design of each element has been obtained, the analysis of the entire focal plane array system can begin. We will focus on its FoV, directivity and bandwidth. Mutual coupling between lenses, which has not been focused on in this study, will also be discussed.

# ACKNOWLEDGEMENTS

I'd want to express my gratitude to a variety of individuals for their contributions to this effort. How blessed I am to have the love and help of so many people.

I would like to convey my heartfelt gratitude to prof. dr. Nuria Llombart Juan, my supervisor. You were always there, waiting for me with such kindness, and you were always prepared to provide a hand when I needed it. Not only did I receive intellectual training from this, but I also received emotional support. Nevertheless, what attracted me most was your rigorous approach and your vast engineering experience. These sparkling lights were like torches that illuminated my confusion. Your professional guidance and constructive comments, as well as your invaluable support and patient patience, make an indelible impression on me as a mature female scholar and engineer, who serves as my role model and aspiration.

I am especially appreciative of the advice provided by dr. Shahab Oddin Dabironezare, my daily supervisor. You are the most excellent mentor I have ever met. You motivated and inspired me to be professional and do the right thing, even when the going got rough. Whatever questions I asked, you always patiently discussed them with me, and I learned a lot during these discussions. You are such an enthusiastic researcher and mentor, and this spirit was infectious to me. Without your tenacious assistance, this project's objective would not have been accomplished.

I would also like to thank all my colleagues in the terahertz group, even though many of them have graduated and moved on. It is a pleasure to work in a group that is so willing to share and communicate.

I'd like to express my gratitude to my parents, who have consistently shown me respect and trust during these years. Your steadfast support has helped me much over my years of school. Additionally, my friends provide me with unwavering support. I am eternally grateful to my good friends globally for being by my side at any hour to help me get through this trying time. I'd want to thank Merel for becoming my first local friend and demonstrating to me how wonderful life is in the Netherlands. I'd want to express my gratitude to Jinghui, Maosheng, Xixi, and Xinyu for looking after me at a difficult time in my health. I'd want to thank Run, Haoyu, Shiting, Mengjin, and other friends for their unwavering support despite the time difference.

Indeed, I would like to express my sincere thanks to my doctors, psychologists, psychotherapists, and general practitioners, without whom I would never be able to complete this thesis. Fortunately, dr. Marion van den Baar, dr. Kirsten Flink, dr. Jack Cieplinski, dr. Lu Wang, and dr. Ping Xu use their kind words, extensive theory, and practical ways to assist me in regaining my equilibrium.

Finally, I want to express my gratitude to myself for always determining the motivation and never giving up. Although it took me twice as long to complete my Master's degree compared to others, I still feel it was worth it. I spent two of those years learning the fundamentals of terahertz and learning how to collaborate with a fantastic group of researchers, and the other two years learning how to get along with myself and make peace with that big black dog. This five-year master journey will be the most remarkable treasure that I will cherish for the rest of my life.

*Muhan Zhang  
Shanghai, 2023*

# LIST OF PUBLICATIONS

1. S. O. Dabironezare, M. Zhang, G. Carluccio, A. Freni, A. Neto and N. Llombart, "Design of a Wide-Scan Lens Based Focal Plane Array for Sub-millimeter Imaging Systems Using Coherent Fourier Optics," *14th European Conference on Antennas and Propagation (EuCAP 2020)*, Copenhagen, Denmark, March 2020, **nominated for the best paper award in antennas category**.
2. S. O. Dabironezare, M. Zhang, G. Carluccio, A. Freni, A. Neto and N. Llombart, "Design of a Wide-Scan Lens based Focal Plane Array using Coherent Fourier Optics," *IEEE Antennas and Propagation International Symposium (APS 2020)*, Montreal, Quebec, Canada, July 2020.
3. H. Zhang, S. O. Dabironezare, M. Zhang and N. Llombart, "Design of Lens Based Focal Plane Arrays for Wide Field-of-View Imagers at Sub-millimeter Wavelengths," *2021 46th International Conference on Infrared, Millimeter and Terahertz Waves (IRMMW-THz)*, Chengdu, China, August 2021.



# REFERENCES

- [1] S. Dabironezare, M. Zhang, G. Carluccio, A. Freni, A. Neto, and N. Llombart, *Design of lens based focal plane arrays for wide field of view imaging using coherent fourier optics*, in *2020 45th International Conference on Infrared, Millimeter, and Terahertz Waves (IRMMW-THz)* (IEEE, 2020) pp. 1–1.
- [2] S. Dabironezare, *Fourier Optics Field Representations for the Design of Wide Field-of-View Imagers at Sub-millimetre Wavelengths*, [Ph.D. thesis](#), Delft University of Technology (2020).
- [3] D. A. Robertson, D. G. Macfarlane, R. I. Hunter, S. L. Cassidy, N. Llombart, E. Gandini, T. Bryllert, M. Ferndahl, H. Lindström, J. Tenhunen, *et al.*, *The consortis 16-channel 340-ghz security imaging radar*, in *Passive and Active Millimeter-Wave Imaging XXI*, Vol. 10634 (International Society for Optics and Photonics, 2018) p. 1063409.
- [4] D. M. Sheen, D. L. McMakin, and T. E. Hall, *Three-dimensional millimeter-wave imaging for concealed weapon detection*, *IEEE Transactions on microwave theory and techniques* **49**, 1581 (2001).
- [5] J. A. Martinez-Lorenzo, F. Quivira, and C. Rappaport, *Sar imaging of suicide bombers wearing concealed explosive threats*, *Progress In Electromagnetics Research* **125**, 255 (2012).
- [6] X. Zhuge and A. G. Yarovoy, *A sparse aperture mimo-sar-based uwb imaging system for concealed weapon detection*, *IEEE Transactions on Geoscience and Remote Sensing* **49**, 509 (2010).
- [7] O. Yurduseven, *Indirect microwave holographic imaging of concealed ordnance for airport security imaging systems*, *Progress in Electromagnetics Research* **146**, 7 (2014).
- [8] D. A. Robertson, S. L. Cassidy, and D. R. Bolton, *Nonlinearity and phase noise effects in 340 ghz 3d imaging radar*, in *Passive and Active Millimeter-Wave Imaging XVI*, Vol. 8715 (SPIE, 2013) pp. 163–172.
- [9] K. B. Cooper, R. J. Dengler, N. Llombart, B. Thomas, G. Chattopadhyay, and P. H. Siegel, *Thz imaging radar for standoff personnel screening*, *IEEE transactions on terahertz science and technology* **1**, 169 (2011).
- [10] D. M. Sheen, T. E. Hall, R. H. Severtsen, D. L. McMakin, B. K. Hatchell, and P. L. Valdez, *Standoff concealed weapon detection using a 350-ghz radar imaging system*,

- in *Passive Millimeter-Wave Imaging Technology XIII*, Vol. 7670 (SPIE, 2010) pp. 57–68.
- [11] C. Am Weg, W. von Spiegel, R. Henneberger, R. Zimmermann, T. Loeffler, and H. G. Roskos, *Fast active thz cameras with ranging capabilities*, *Journal of Infrared, Millimeter, and Terahertz Waves* **30**, 1281 (2009).
- [12] D. A. Robertson, P. N. Marsh, D. R. Bolton, R. J. Middleton, R. I. Hunter, P. J. Speirs, D. G. Macfarlane, S. L. Cassidy, and G. M. Smith, *340-ghz 3d radar imaging test bed with 10-hz frame rate*, in *Passive and Active Millimeter-Wave Imaging XV*, Vol. 8362 (SPIE, 2012) pp. 41–51.
- [13] M. Elsdon, O. Yurduseven, and D. Smith, *Early stage breast cancer detection using indirect microwave holography*, *Progress In Electromagnetics Research* **143**, 405 (2013).
- [14] N. K. Nikolova, *Microwave imaging for breast cancer*, *IEEE microwave magazine* **12**, 78 (2011).
- [15] Y. Wang and A. E. Fathy, *Advanced system level simulation platform for three-dimensional uwb through-wall imaging sar using time-domain approach*, *IEEE Transactions on Geoscience and Remote Sensing* **50**, 1986 (2011).
- [16] T. S. Ralston, G. L. Charvat, and J. E. Peabody, *Real-time through-wall imaging using an ultrawideband multiple-input multiple-output (mimo) phased array radar system*, in *2010 IEEE international symposium on phased array systems and technology* (IEEE, 2010) pp. 551–558.
- [17] S. Caorsi, A. Massa, M. Pastorino, and M. Donelli, *Improved microwave imaging procedure for nondestructive evaluations of two-dimensional structures*, *IEEE Transactions on Antennas and Propagation* **52**, 1386 (2004).
- [18] S. Kharkovsky and R. Zoughi, *Microwave and millimeter wave nondestructive testing and evaluation-overview and recent advances*, *IEEE Instrumentation & Measurement Magazine* **10**, 26 (2007).
- [19] P. H. Siegel, *Terahertz technology*, *IEEE Transactions on microwave theory and techniques* **50**, 910 (2002).
- [20] K. B. Cooper and G. Chattopadhyay, *Submillimeter-wave radar: Solid-state system design and applications*, *IEEE microwave magazine* **15**, 51 (2014).
- [21] O. Yurduseven, K. Cooper, and G. Chattopadhyay, *Point-spread-function (psf) characterization of a 340-ghz imaging radar using acoustic levitation*, *IEEE Transactions on Terahertz Science and Technology* **9**, 20 (2018).
- [22] O. Yurduseven, T. Fromenteze, K. Cooper, G. Chattopadhyay, and D. R. Smith, *From microwaves to submillimeter waves: modern advances in computational imaging, radar, and future trends*, in *Terahertz, RF, Millimeter, and Submillimeter-Wave Technology and Applications XII*, Vol. 10917 (SPIE, 2019) pp. 134–144.

- [23] A. Garcia-Pino, N. Llombart, B. Gonzalez-Valdes, and O. Rubinos-Lopez, *A bifocal ellipsoidal gregorian reflector system for thz imaging applications*, IEEE Transactions on Antennas and Propagation **60**, 4119 (2012).
- [24] E. Gandini, J. Svedin, T. Bryllert, and N. Llombart, *Optomechanical system design for dual-mode stand-off submillimeter wavelength imagers*, IEEE Transactions on Terahertz Science and Technology **7**, 393 (2017).
- [25] K. B. Cooper, T. A. Reck, C. Jung-Kubiak, C. Lee, J. V. Siles, R. H. Lin, A. Peralta, E. Decrossas, E. T. Schlecht, G. Chattopadhyay, *et al.*, *Transceiver array development for submillimeter-wave imaging radars*, in *Passive and Active Millimeter-Wave Imaging XVI*, Vol. 8715 (SPIE, 2013) pp. 76–83.
- [26] K. B. Cooper, R. J. Dengler, N. Llombart, T. Bryllert, G. Chattopadhyay, E. Schlecht, J. Gill, C. Lee, A. Skalare, I. Mehdi, *et al.*, *Penetrating 3-d imaging at 4-and 25-m range using a submillimeter-wave radar*, IEEE Transactions on Microwave Theory and Techniques **56**, 2771 (2008).
- [27] E. Commission, *Concealed objects stand-off real-time imaging for security*, <https://cordis.europa.eu/project/id/312745/reporting> (2023).
- [28] D. A. Robertson, D. G. Macfarlane, R. I. Hunter, S. L. Cassidy, N. Llombart, E. Gandini, T. Bryllert, M. Ferndahl, H. Lindström, J. Tenhunen, *et al.*, *High resolution, wide field of view, real time 340ghz 3d imaging radar for security screening*, in *Passive and Active Millimeter-Wave Imaging XX*, Vol. 10189 (SPIE, 2017) pp. 83–91.
- [29] D. A. Robertson, S. L. Cassidy, B. Jones, and A. Clark, *Concealed threat detection with the irad sub-millimeter wave 3d imaging radar*, in *Passive and Active Millimeter-Wave Imaging XVII*, Vol. 9078 (SPIE, 2014) pp. 28–34.
- [30] N. Llombart, B. Blázquez, A. Freni, and A. Neto, *Fourier optics for the analysis of distributed absorbers under thz focusing systems*, IEEE Transactions on Terahertz Science and Technology **5**, 573 (2015).
- [31] N. Llombart, S. O. Dabironezare, G. Carluccio, A. Freni, and A. Neto, *Reception power pattern of distributed absorbers in focal plane arrays: A fourier optics analysis*, IEEE Transactions on Antennas and Propagation **66**, 5990 (2018).
- [32] S. O. Dabironezare, G. Carluccio, A. Freni, A. Neto, and N. Llombart, *Coherent fourier optics model for the synthesis of large format lens-based focal plane arrays*, IEEE Transactions on Antennas and Propagation **69**, 734 (2020).
- [33] N. J. McEwan and P. F. Goldsmith, *Gaussian beam techniques for illuminating reflector antennas*, IEEE transactions on antennas and propagation **37**, 297 (1989).
- [34] E. Gandini, A. Tamminen, A. Luukanen, and N. Llombart, *Wide field of view inversely magnified dual-lens for near-field submillimeter wavelength imagers*, IEEE Transactions on Antennas and Propagation **66**, 541 (2017).

- [35] N. Llombart, A. Neto, G. Gerini, M. Bonnedal, and P. De Maagt, *Impact of mutual coupling in leaky wave enhanced imaging arrays*, IEEE Transactions on Antennas and Propagation **56**, 1201 (2008).
- [36] M. A. Campo, D. Blanco, S. Bruni, A. Neto, and N. Llombart, *On the use of fly's eye lenses with leaky-wave feeds for wideband communications*, IEEE Transactions on Antennas and Propagation **68**, 2480 (2020).
- [37] M. Arias Campo, *On the Design of Fly's Eye Lenses at Sub-THz Frequencies for Wideband Communications*, [Ph.D. thesis](#), Delft University of Technology (2021).
- [38] S. Bosma, A. Neto, and N. Llombart, *On the near-field spherical wave formation in resonant leaky-wave antennas: Application to small lens design*, IEEE Transactions on Antennas and Propagation **70**, 801 (2021).
- [39] A. W. Rudge and M. J. Withers, *New technique for beam steering with fixed parabolic reflectors*, (1971).
- [40] V. Galindo-Israel, S.-W. Lee, and R. Mittra, *Synthesis of a laterally displaced cluster feed for a reflector antenna with application to multiple beams and contoured patterns*, IEEE Transactions on Antennas and Propagation **26**, 220 (1978).
- [41] C. Hung and G. Chadwick, *Corrected off axis beams for parabolic reflectors*, APS, 278 (1979).
- [42] J. F. Johansson, *A comparison of some feed types*, in *Multi-Feed Systems for Radio Telescopes*, Vol. 75 (1995) pp. 82–89.
- [43] Z. von F, *Beugungstheorie des schneidenver-fahrens und seiner verbesserten form, der phasenkontrastmethode*, physica **1**, 689 (1934).
- [44] A. Prata and W. Rusch, *A quadrature formula for evaluating zernike polynomial expansion coefficients (antenna analysis)*, in *Digest on Antennas and Propagation Society International Symposium* (IEEE, 1989) pp. 1174–1177.
- [45] H. Zhang, S. O. Dabironezare, M. Zhang, and N. Llombart, *Design of lens based focal plane arrays for wide field-of-view imagers at sub-millimeter wavelengths*, in *2021 46th International Conference on Infrared, Millimeter and Terahertz Waves (IRMMW-THz)* (IEEE, 2021) pp. 1–2.
- [46] S. O. Dabironezare, M. Zhang, G. Carluccio, A. Freni, and N. Llombart, *Design of lens based focal plane arrays for wide field of view imaging using coherent fourier optics*, in *2020 45th International Conference on Infrared, Millimeter and Terahertz Waves (IRMMW-THz)* (IEEE, 2020) pp. 1–1.